

A rehomogenization-based approach to model spectral effects of local nuclide density changes in nodal calculations

Gamarino, Matteo; Dall'Osso, Aldo; Lathouwers, Danny; Kloosterman, Jan Leen

DOI

[10.1016/j.anucene.2018.10.061](https://doi.org/10.1016/j.anucene.2018.10.061)

Publication date

2019

Document Version

Final published version

Published in

Annals of Nuclear Energy

Citation (APA)

Gamarino, M., Dall'Osso, A., Lathouwers, D., & Kloosterman, J. L. (2019). A rehomogenization-based approach to model spectral effects of local nuclide density changes in nodal calculations. *Annals of Nuclear Energy*, 126, 142-168. <https://doi.org/10.1016/j.anucene.2018.10.061>

Important note

To cite this publication, please use the final published version (if applicable). Please check the document version above.

Copyright

Other than for strictly personal use, it is not permitted to download, forward or distribute the text or part of it, without the consent of the author(s) and/or copyright holder(s), unless the work is under an open content license such as Creative Commons.

Takedown policy

Please contact us and provide details if you believe this document breaches copyrights. We will remove access to the work immediately and investigate your claim.



Contents lists available at ScienceDirect

Annals of Nuclear Energy

journal homepage: www.elsevier.com/locate/anucene

A rehomogenization-based approach to model spectral effects of local nuclide density changes in nodal calculations



Matteo Gamarino ^{a,*}, Aldo Dall'Osso ^b, Danny Lathouwers ^a, Jan Leen Kloosterman ^a

^a Delft University of Technology, Department of Radiation, Science and Technology, Mekelweg 15, 2629 JB Delft, The Netherlands

^b Framatome, Tour AREVA, 92084 Paris La Défense Cedex, France

ARTICLE INFO

Article history:

Received 24 May 2018

Received in revised form 25 October 2018

Accepted 30 October 2018

Keyword:

Nodal methods

Homogenization

Cross-section model

State parameters

Spectral changes

Leakage

ABSTRACT

In reactor core nodal analysis, the dependence of few-group, homogenized cross sections on the local physical conditions (i.e., the thermal-hydraulic state and material composition) is commonly represented via multivariate interpolation in parameterized libraries. In this paper, we propose a novel approach to model the spectral effects of changes in the moderator density and in the concentrations of diluted boron and xenon. This method is based on the spectral rehomogenization technique developed at Framatome and TU Delft to account for neighbor effects on the nodal cross sections. We compute on the fly the variation in the infinite-medium energy-collapsing spectrum from a nominal state to a perturbed condition (i.e., with different values of the aforementioned state parameters). The dependence of the microscopic and macroscopic cross sections on these three variables is thus resolved without the standard multidimensional interpolation. This strategy reduces substantially the computational burden of the lattice calculation, the cross-section library memory requirements, and the run time of the on-line cross-section reconstruction.

The proposed approach is applied to a pressurized-water-reactor UO₂ fuel assembly at zero burn-up, covering a wide range of the values of the water density and of the concentrations of boron and xenon. Both normal and abnormal operating conditions are considered. We show that, in most cases, cross-section changes are predicted with an accuracy comparable to that of traditional interpolation. Higher errors (but reasonably small compared to the range of accuracy of nodal computational tools) are only found at very low moderator densities, typical of accidental conditions. As further validation of the methodology, we simulate a heterogeneous multiassembly configuration. With this benchmark problem, we prove that the method can reconstruct the spectrum variation between the real environment in a perturbed state and the infinite lattice in the nominal one, thus modeling simultaneously the non-separable spectral effects of local physical conditions and internodal neutron leakage.

© 2018 The Author(s). Published by Elsevier Ltd. This is an open access article under the CC BY license (<http://creativecommons.org/licenses/by/4.0/>).

1. Introduction

Light Water Reactor (LWR) full-core analysis for industrial applications is usually performed with advanced nodal diffusion codes (Lawrence, 1986; Stacey, 2007). Nodal cross sections are obtained from flux-weighted spatial homogenization and energy condensation in detailed neutron transport calculations for each fuel-assembly type (Smith, 1986; Sanchez, 2009). The fuel lattice is generally modeled with the infinite-medium approximation (i.e., reflective boundary conditions at the assembly outer edges). The energy distribution of the neutron flux spectrum used for few-group collapsing depends on the thermal-hydraulic conditions

and the material composition in the node. Therefore, input cross sections for nodal codes must be represented as a function of the local, instantaneous physical conditions. For Pressurized Water Reactors (PWRs), the following variables (referred to as state parameters) are commonly chosen for the representation: the burn-up, the fuel temperature, the moderator/coolant temperature, the moderator/coolant density, the concentration of boric acid (¹⁰B) dissolved in the moderator, and the concentration of xenon (¹³⁵Xe). An additional parameter is the presence of control rods. Boiling Water Reactor (BWR) modeling calls for a somewhat more detailed set of state parameters. For example, the following instantaneous variables are considered in Framatome's nodal code ARTEMIS (Hobson et al., 2013; Martin et al., 2017): the burn-up, the fuel temperature, the instantaneous coolant void fraction, the instantaneous moderator void fraction, the moderator temperature (for cold start-up conditions), the xenon concentration, the

* Corresponding author.

E-mail addresses: matteo.gamarino@gmail.com (M. Gamarino), J.L.Kloosterman@tudelft.nl (J.L. Kloosterman).

instantaneous presence of control blades, and water-gap dimension changes due to channel bow. In other BWR core simulators, the void fraction is replaced by the temperatures and densities of both moderator and coolant, with the density responding to void or pressure changes. The concentration of soluble boron (which is not used for shim control in BWRs) is often also retained for safety/transient calculations, such as the Anticipated Transient Without Scram (ATWS).

Spectral effects due to deviations between the actual core depletion and the single-assembly base depletion may be accounted for with empirically-defined history variables (Watson et al., 2002; Bilodid and Mittag, 2010). These include the local concentration of ^{239}Pu , the spectral-history index, the burnable-poison history (for PWRs), the control-blade history (for BWRs), and the coolant void or density history (for BWRs). However, modern nodal codes make use of microscopic depletion models to track the evolution of a number of nuclides (Bilodid and Mittag, 2010), thus discarding history variables in the cross-section parameterization of PWRs. With these microscopic models, only the control-blade history and the density history must be kept in the cross-section model of BWRs because of the high sensitivity of the intranodal heterogeneous flux distribution (namely, the lattice code flux) to the presence of control blades and void. The tabulation of these two parameters may become unnecessary in more advanced methodologies that make use of a spatially detailed (i.e., semi-heterogeneous) submesh approach for on-line homogenization of the macroscopic and microscopic cross sections (Bahadir et al., 2005; Bahadir and Lindahl, 2009).

The lattice calculations are performed for a limited set of reactor states, from which a continuous representation (namely, the cross-section library) is built to cover the whole state-parameter phase space. In this way, nodal cross sections can be reconstructed at the exact, local conditions during the on-line core calculation. The library generation depends on (i) the model chosen for the representation of multivariate dependences, and (ii) the state-parameter sampling strategy. These two aspects are briefly reviewed in the following.

It is common practice to represent the cross-section functional dependence by interpolation or approximation methods (Zimin et al., 2005). In both approaches, the mesh for the multidimensional domain is composed of the linear subspaces of the single independent variables (i.e., the axes or directions). For each axis, a functional basis is found. A generic multivariate function is built by a linear combination of tensor products of the one-dimensional basis functions. In the interpolation approach (Watson et al., 2002), the cross sections at a given state (i.e., a point inside the tensorized grid) are computed based on the mesh-point values with a linear or higher-order (polynomial, spline) interpolation algorithm. For instance, in ARTEMIS the interpolation functions for PWR cores are combinations of cubic B-splines (for the burn-up and moderator density) and second-order polynomials (for the other state variables). Four triplets (namely, three-parameter cross terms) are used to build the multivariate dependence. The interpolation approach is very general, because it demands no knowledge of the functional dependence of the interpolated data. However, it suffers from three main downsides (Zimin et al., 2005; Bokov, 2009): (i) it does not support a direct extrapolation of cross sections at operating points beyond the mesh boundaries, (ii) it requires a regular Cartesian mesh, and (iii) it is prone to the *curse of dimensionality*. The second point may hamper the definition of an optimal grid, because certain state parameters are more important than others in the cross-section representation. Regions of little or no physical interest may be included in the tabulation, causing a worthless increase in the number of lattice calculations and in the size of the cross-section library. The third drawback, typical of high-dimensional systems, is because the number of

mesh points and the computational cost of library generation grow exponentially with the number of state parameters (Bokov, 2009). This aspect strongly penalizes the simulation of reactor transients and design basis accidents, for which cross-section libraries must span wider intervals of the state parameters than in ordinary operating conditions.

Approximation techniques aim to estimate cross-term dependences by functional forms (Zimin et al., 2005). Since few-group, homogenized cross sections mostly exhibit a smooth behavior versus the state parameters, polynomial functions are usually employed. Functional relations between the single cross sections and the state parameters are not known *a priori*. The main challenge is therefore finding an optimal multivariate polynomial for each cross-section type. Several strategies to identify suitable polynomials are described in the literature. Among them, we mention trial-and-error approaches (Turski et al., 1997), stepwise regression (Zimin et al., 2005), quasi-regression (Bokov and Prinsloo, 2007; Bokov et al., 2008; Bokov, 2009), regression (Dufek, 2011), and the Tucker decomposition (Luu et al., 2017). With approximation techniques, there is no restriction on the type of grid. Unstructured multivariate domains are used, with an appreciable reduction in the number of mesh points and lattice simulations. Extrapolation outside the mesh boundaries is easily performed. Moreover, the so obtained cross-section libraries only contain the regression coefficients. They have, therefore, significantly smaller size than the parameterized tables ensuing from the interpolation approach (Zimin et al., 2005; Dufek, 2011). However, this strategy is also affected by the curse of dimensionality, because the number of important polynomials increases dramatically if many state variables are considered. Furthermore, since a polynomial function must be determined for each type of macroscopic and microscopic cross sections, the regression cost may be high.

When building the cross-section model (by either interpolation or approximation), the sampling strategy is also of great importance for the accuracy and effectiveness of the representation. Quasi-random sampling is used in several polynomial-regression approaches (Zimin et al., 2005; Bokov et al., 2008; Bokov, 2009; Dufek, 2011). Sánchez-Cervera et al. (2014) employed first-order adjoint perturbation theory to evaluate the sensitivity of the infinite-medium multiplication factor (k_{∞}) to the distance between points in the interpolation grid. For each axis, they estimated the optimal intervals between samples and their minimum number to satisfy a given target accuracy in k_{∞} . Recently, an increasing interest has been shown in sparse-grid methods (Botes and Bokov, 2011; Bokov et al., 2012; Botes and Bokov, 2014; Botes et al., 2017). This approach consists of sampling the state-parameter phase space on a reduced tensor-product grid. Sparse-grid sampling was investigated in the framework of both interpolation and regression approaches. For example, Botes and Bokov (2011) showed that, for a linear interpolation algorithm, a sparse grid requires orders of magnitude fewer points than a full tensor-product grid, while satisfying the same target accuracy.

Current methods for the generation of nodal data are also hampered by homogenization errors. These errors are caused by deviations of the neutron flux distribution in the real environment from the infinite-medium flux used for cross-section weighting at the lattice-calculation stage. Such sources of inaccuracy can hinder an accurate simulation of strongly heterogeneous systems, where interassembly streaming effects are relevant. Typical examples are fuel loading strategies with low-enriched uranium and mixed-oxide (MOX) assemblies, layouts with control-rod banks inserted, and core designs with local burnable absorbers (such as Pyrex and gadolinium). In these configurations, environmental effects must be taken into account to predict reliable estimates of the reaction rates and multiplication factor. A review of methods to incorporate this kind of effect can be found in Gamarino et al. (2018a).

The work presented in this paper aims to mitigate some of the weaknesses of the cross-section methodology discussed hitherto. We describe a novel approach to model the spectral effects of three relevant state parameters: the moderator/coolant density (ρ_{H_2O}), the soluble-boron concentration ($C_{B_{10}}$), and the xenon concentration ($N_{Xe_{135}}$). Our work is an original development of the spectral rehomogenization technique described in [Dall'Osso et al. \(2010\)](#) and [Gamarino et al. \(2018a,b\)](#). This method has been applied successfully to correct on the fly the spectral component of the homogenization defect due to dissimilar neighbor assemblies. In this paper, we extend the methodology to compute the variation in the infinite-medium condensation spectrum caused by local nuclide density perturbations. Changes in the fine-energy homogenized cross sections are incorporated by a heuristic approach. We show that the dependence of the few-group, macroscopic and microscopic cross sections on the aforementioned state variables (ρ_{H_2O} , $C_{B_{10}}$, and $N_{Xe_{135}}$) can be accounted for directly. Neither multivariate interpolation in the parameterized libraries nor multidimensional polynomial approximation is needed along these three axes of the state-parameter phase space, which can be eliminated or sampled individually (namely, without cross terms) at far fewer points. This strategy reduces (i) the computational burden of the lattice-physics calculation (i.e., the number of reactor states to be simulated), (ii) the size of the cross-section libraries, and (iii) the run time of the nodal-data reconstruction during the on-line calculation.

This paper is organized as follows. The method is described in Section 2. In Section 3, we show the numerical results of various test cases. We first validate the methodology on single-assembly configurations. We consider a typical PWR UO₂ fuel assembly at zero burn-up. The accuracy of the cross-section reconstruction is tested for a broad range of the values of the three state parameters considered in this work. Afterwards, we investigate a heterogeneous PWR multiassembly configuration hosting control rods. In this benchmark problem, the method is applied to capture the combined spectral effects of perturbations in the local physical conditions and interassembly neutron streaming. In Section 4 we discuss several aspects of interest of the methodology, such as its main numerical features and the benefits on the cross-section model. We also address the impact of variations in the state parameters on the assembly discontinuity factors and on the form functions for the pin-power reconstruction. Conclusions are drawn in Section 5.

2. Description of the method

In Section 2.1 we describe the method to reconstruct the infinite-medium macroscopic and microscopic nodal cross sections. In Section 2.2 we show how neighbor effects ([Gamarino et al., 2018a,b](#)) can be incorporated into this procedure.

2.1. Reconstruction of the infinite-medium cross sections

The proposed reconstruction method can be applied to both types of cross-section models reviewed in Section 1. In this work, we focus on the interpolation technique. This is currently the most widely used approach in core simulators ([Bahadir and Lindahl, 2009](#); [Hobson et al., 2013](#); [Guillo et al., 2017](#)). The derivation that follows focuses on the PWR technology. Some considerations about other types of reactors (such as BWRs) are made in Section 4.1.

We define the following set of state parameters (for a PWR):

$$p = [Bu, T_{\text{fuel}}, T_{H_2O}, N_{H_2O}, N_{B_{10}}, N_{Xe_{135}}], \quad (1)$$

denoting, in order, the burn-up, the fuel temperature, the water temperature, the molecular number density of water, and the

atomic number densities of diluted boron and xenon. The water mass density ρ_{H_2O} (in g/cm³) and the boron concentration $C_{B_{10}}$ (in parts per million - ppm) are linearly related to the corresponding number densities:

$$\rho_{H_2O} = N_{H_2O} m_{H_2O} \frac{10^{24}}{N_{Av}}, \quad C_{B_{10}} = \frac{N_{B_{10}}}{\rho_{H_2O}} \frac{m_{B_{10}}}{f_{B_{10}}} \frac{10^{24}}{N_{Av}} 10^6, \quad (2)$$

where m_{H_2O} is the water molecular weight, $m_{B_{10}}$ is the atomic weight of the isotope ¹⁰B, $f_{B_{10}}$ is the mass fraction of ¹⁰B in the boron mixture, and N_{Av} is the Avogadro number.

In standard approaches, the infinite-medium macroscopic cross section $\Sigma_{x,G}^\infty$ (for a given reaction type x and the coarse energy group G) is reconstructed at the local physical conditions in a node (p_{loc}) as follows:

$$\Sigma_{x,G}^\infty(p_{loc}) = \Sigma_{x,G}^{\infty, \text{res}}(p_{loc}) + \sum_{c=1}^{n_I} N_c^{\text{loc}} \sigma_{x,c,G}^\infty(p_{loc}). \quad (3)$$

In Eq. (3), n_I is the number of isotopes tracked by the cross-section model; N_c^{loc} is the local number density of isotope c ; $\sigma_{x,c,G}^\infty$ is the coarse-group microscopic cross section of isotope c ; and $\Sigma_{x,G}^{\infty, \text{res}}$ is the residual (i.e., lumped) macroscopic cross section, carrying the contribution of the isotopes that are not modeled explicitly. All quantities in Eq. (3) are spatially homogenized in the node. The cross sections $\sigma_{x,c,G}^\infty$ and $\Sigma_{x,G}^{\infty, \text{res}}$ are interpolated in the parameterized libraries at the local values of the variables listed in Eq. (1). The densities N_c^{loc} are taken as input from the thermal-hydraulic feedback and fuel depletion calculations (and, possibly, from a critical-boron search for $N_{B_{10}}$).

We introduce a reduced set of state parameters, p' :

$$p' = [Bu, T_{\text{fuel}}, T_{H_2O}]. \quad (4)$$

This subset defines a tensorized grid made of only three axes (instead of six), with the densities N_{H_2O} , $N_{B_{10}}$ and $N_{Xe_{135}}$ kept fixed at a reference nominal value ($N_{H_2O}^{\text{nom}}$, $N_{B_{10}}^{\text{nom}}$, and $N_{Xe_{135}}^{\text{nom}}$) when building the cross-section interpolation tables. Using this reduced set and introducing a correction term $\delta\Sigma_{x,G}^\infty$, Eq. (3) is rewritten as

$$\Sigma_{x,G}^\infty(p_{loc}) = \Sigma_{x,G}^{\infty, \text{res}}(p'_{loc}) + \sum_{c=1}^{n_I} N_c^{\text{loc}} \sigma_{x,c,G}^\infty(p'_{loc}) + \delta\Sigma_{x,G}^\infty. \quad (5)$$

The cross sections $\sigma_{x,c,G}^\infty$ and $\Sigma_{x,G}^{\infty, \text{res}}$ are now only interpolated at the local burn-up, fuel temperature and water temperature. The spectral effect of changes in N_{H_2O} , $N_{B_{10}}$ and $N_{Xe_{135}}$ from their nominal values is taken into account with the additional term $\delta\Sigma_{x,G}^\infty$. This correction is computed on the fly (namely, during the nodal calculation) by an iterative procedure, which we address below.

We define the local (p_{loc}) and nominal (p_{nom}) conditions as

$$p_{loc} = [p'_{loc}, N_{H_2O}^{\text{loc}}, N_{B_{10}}^{\text{loc}}, N_{Xe_{135}}^{\text{loc}}] \quad (6a)$$

and

$$p_{nom} = [p'_{loc}, N_{H_2O}^{\text{nom}}, N_{B_{10}}^{\text{nom}}, N_{Xe_{135}}^{\text{nom}}]. \quad (6b)$$

Table 1 shows the nominal values of ρ_{H_2O} , $C_{B_{10}}$ and $N_{Xe_{135}}$ that have been chosen in this work. The selected value of $N_{Xe_{135}}^{\text{nom}}$ is about twice as high as the the average xenon concentration in the depletion of a highly-enriched UO₂ fuel assembly. This choice is meant to consider an intermediate value between the equilibrium concentration in a standard power reactor and the peak values occurring at the extreme points of a spatial neutron oscillation ([Duderstadt and Hamilton, 1976](#)).

Changes in ρ_{H_2O} , $C_{B_{10}}$ and $N_{Xe_{135}}$ (i.e., transitions from p_{nom} to p_{loc}) have three different effects on $\Sigma_{x,G}^\infty$:

Table 1

Nominal values of the moderator/coolant density ($\rho_{H_2O}^{nom}$), the soluble-boron concentration ($C_{B_{10}}^{nom}$), and the xenon atomic density ($N_{Xe_{135}}^{nom}$). The xenon density is expressed in atoms/cubic Ångström ($\text{a}/\text{Å}^3$).

State parameter	Nominal value
$\rho_{H_2O}^{nom}$	0.7 g/cm ³
$C_{B_{10}}^{nom}$	700 ppm
$N_{Xe_{135}}^{nom}$	$4.0 \cdot 10^{-9}$ a/Å ³

- a *direct* effect, due to variations in the corresponding number densities;
- a spectral effect, due to variations in the infinite-medium condensation spectrum;
- a third effect, due to perturbations in the fine-energy microscopic cross-section distributions [$\sigma_{\infty,x,c}(E)$] that are collapsed to few groups via spectrum weighting.

We refer to the third effect as *microscopic* effect. The direct effect is trivially taken into account using the actual local densities ($N_{H_2O}^{loc}$, $N_{B_{10}}^{loc}$ and $N_{Xe_{135}}^{loc}$) in Eq. (5). The spectral and microscopic effects act upon the few-group residual and isotopic cross sections. We search an analytic expression to model these effects starting from the definition of the generic isotopic cross section $\sigma_{x,c,G}^{\infty}$ condensed in the exact, local conditions. This reads

$$\sigma_{x,c,G}^{\infty,loc} = \frac{1}{\bar{\Phi}_{\infty,G}^{loc}} \int_{E_G^-}^{E_G^+} dE \sigma_{\infty,x,c}^{loc}(E) \Phi_{\infty}^{loc}(E), \quad (7)$$

where $\bar{\Phi}_{\infty,G}^{loc}$ is the few-group flux, $\sigma_{\infty,x,c}^{loc}(E)$ is the microscopic cross-section energy distribution, and $\Phi_{\infty}^{loc}(E)$ is the condensation spectrum. All quantities in Eq. (7) are homogenized in the infinite lattice. The limits of integration E_G^- and E_G^+ denote the G^{th} -group lower and upper energy boundaries, respectively. We introduce a non-dimensional lethargy-like variable u , which is defined separately in each coarse group with bounds 0 and 1 (Gamarino et al., 2018a):

$$u_G(E) = \frac{\ln\left(\frac{E}{E_G^-}\right)}{\ln\left(\frac{E_G^+}{E_G^-}\right)}. \quad (8)$$

We define the condensation spectrum in the local conditions in the domain of u (from now on we will omit the subscript G when referring to u) as

$$\Phi_{\infty,G}^{loc}(u) = \bar{\Phi}_{\infty,G}^{loc} \varphi_{\infty,G}^{nom}(u) + \delta\Phi_{\infty,G}(u), \quad (9)$$

where $\varphi_{\infty,G}^{nom}(u)$ is the reference condensation spectrum (normalized to unity) in the nominal conditions, and $\delta\Phi_{\infty,G}(u)$ is the spectrum change due to perturbations in ρ_{H_2O} , $C_{B_{10}}$ and $N_{Xe_{135}}$ (i.e., the spectrum change that occurs when moving from p_{nom} to p_{loc}). A similar equation is introduced for $\sigma_{\infty,x,c}^{loc}(E)$:

$$\sigma_{\infty,x,c,G}^{loc}(u) = \sigma_{\infty,x,c,G}^{nom}(u) + \delta\sigma_{\infty,x,c,G}(u). \quad (10)$$

Moving from E to u and introducing Eqs. (9) and (10) into Eq. (7), we obtain

$$\sigma_{x,c,G}^{\infty,loc} = \sigma_{x,c,G}^{\infty,nom} + \delta\sigma_{x,c,G}^{\infty,s} + \delta\sigma_{x,c,G}^{\infty,m} + \delta\sigma_{x,c,G}^{\infty,*}, \quad (11)$$

where we have defined

- the few-group isotopic cross section in the nominal conditions:

$$\sigma_{x,c,G}^{\infty,nom} = \int_0^1 du \sigma_{\infty,x,c,G}^{nom}(u) \varphi_{\infty,G}^{nom}(u); \quad (12a)$$

- the isotopic correction term due to the spectral effect:

$$\delta\sigma_{x,c,G}^{\infty,s} = \frac{1}{\bar{\Phi}_{\infty,G}^{loc}} \int_0^1 du \sigma_{\infty,x,c,G}^{nom}(u) \delta\Phi_{\infty,G}(u); \quad (12b)$$

- the isotopic correction term due to the microscopic effect:

$$\delta\sigma_{x,c,G}^{\infty,m} = \int_0^1 du \delta\sigma_{\infty,x,c,G}(u) \varphi_{\infty,G}^{nom}(u); \quad (12c)$$

- a cross (i.e., spectral-microscopic) isotopic correction term:

$$\delta\sigma_{x,c,G}^{\infty,*} = \frac{1}{\bar{\Phi}_{\infty,G}^{loc}} \int_0^1 du \delta\sigma_{\infty,x,c,G}(u) \delta\Phi_{\infty,G}(u). \quad (12d)$$

During the nodal simulation, the nominal cross section $\sigma_{x,c,G}^{\infty,nom}$ (Eq. (12a)) is interpolated in the parameterized libraries at the local values of Bu , T_{fuel} and T_{H_2O} . The iterative calculation of the cross-section corrections of Eqs. (12b)–(12d) is addressed in Sections 2.1.1 and 2.1.2. In Section 2.1.3 we show how the macroscopic correction $\delta\Sigma_{x,G}^{\infty}$ (Eq. (5)) can be computed at each iteration step and provide a global overview of the methodology.

2.1.1. The spectral effect

The variation in the condensation spectrum due to local nuclide density changes is estimated following the approach described in Gamarino et al. (2018a) for the environmental spectrum correction, with some different assumptions.

We consider the continuous-energy neutron balance equation in the infinite lattice at the local conditions. In the lethargy-like domain, this reads

$$\Sigma_{\infty,t,G}^{loc}(u) \Phi_{\infty,G}^{loc}(u) = \sum_{G'=1}^{N_G} \left(\frac{\chi_G(u)}{k_{\infty}^{loc}} \int_0^1 du' \nu \Sigma_{\infty,f,G'}^{loc}(u') \Phi_{\infty,G'}^{loc}(u') + \int_0^1 du' \Sigma_{\infty,s,G'-G}^{loc}(u' \rightarrow u) \Phi_{\infty,G'}^{loc}(u') \right), \quad (13)$$

where N_G denotes the number of coarse energy groups and k_{∞}^{loc} is the single-assembly multiplication factor. We neglect the dependence of the neutron fission-emission spectrum $\chi_G(u)$ on the local conditions. This approximation is acceptable, because the fission spectrum is mainly influenced by the fuel composition and enrichment (Lamarsh, 1966). Eq. (13) is valid in the general case without critical-buckling correction on the nodal cross sections. If a critical-spectrum search is made in the lattice-physics calculation, the following leakage rate must be added to the left-hand side of Eq. (13) (Hebert, 2009):

$$L_{\infty,G}^{loc}(u) = D_{\infty,G}^{loc}(u) B_{crit,loc}^2 \psi_{\infty,G}^{loc}(u), \quad (14)$$

where $B_{crit,loc}^2$ is the buckling coefficient enforcing criticality in the local conditions (commonly determined via the homogeneous fundamental-mode B_1 model), $D_{\infty,G}^{loc}(u)$ is the leakage-coefficient distribution (function of $B_{crit,loc}^2$), and $\psi_{\infty,G}^{loc}(u)$ is the critical spectrum.

Moreover, k_{∞}^{loc} must be set to unity on the right-hand side of Eq. (13). The critical-buckling approach complicates the solution of the rehomogenization problem applied to Eq. (13), because the leakage function detailed in Eq. (14) also depends on the local conditions. In previous work (Gamarino et al., 2018a,b), we showed that our rehomogenization method inherently models the spectrum changes due to different reactivity in the core environment and in the infinite lattice (for instance, criticality in the former and non-criticality in the latter). This feature makes the B_{crit}^2 correction unnecessary. Therefore, in the rest of the derivation we will consider the non-critical medium (Eq. (13)). Some observations about the critical approach will be made in Section 4.5.

We express the spectrum variation $\delta\Phi_{\infty,G}(u)$ (Eq. (9)) as a linear combination of basis functions $Q_{G,i}(u)$:

$$\delta\Phi_{\infty,G}(u) = \sum_{i=1}^{N_{Q_G}} \alpha_{\infty,G,i} Q_{G,i}(u), \quad (15)$$

where N_{Q_G} is the number of modes for the expansion in group G . The modal coefficients $\alpha_{\infty,G,i}$ are determined such that Eq. (13) is satisfied in a weighted-integral sense. After substituting Eqs. (9) and (15) into Eq. (13), we project Eq. (13) on a set of weighting operators $W_{G,j}(u)$, with $j \in [1, N_{Q_G}]$. A linear system of equations is obtained:

$$\begin{aligned} & \bar{\Phi}_{\infty,G}^{\text{loc}} h_{R,r,G,j}^{\text{loc}} + \sum_{i=1}^{N_{Q_G}} \alpha_{\infty,G,i} h_{V,r,G,i,j}^{\text{loc}} \\ &= \frac{\chi_{G,j}}{k_{\infty}^{\text{loc}}} \sum_{G'=1}^{N_G} \left(\bar{\Phi}_{\infty,G'}^{\text{loc}} h_{R,f,G'}^{\text{loc}} + \sum_{i=1}^{N_{Q_{G'}}} \alpha_{\infty,G',i} h_{V,f,G',i}^{\text{loc}} \right) \\ &+ \sum_{\substack{G'=1 \\ G' \neq G}}^{N_G} \left(\bar{\Phi}_{\infty,G'}^{\text{loc}} h_{R,s,G' \rightarrow G,j}^{\text{loc}} + \sum_{i=1}^{N_{Q_{G'}}} \alpha_{\infty,G',i} h_{V,s,G' \rightarrow G,i,j}^{\text{loc}} \right), \end{aligned} \quad (16)$$

with the following expressions for

- the reference rehomogenization coefficients ($h_{R,x,G,j}^{\text{loc}}$):

$$h_{R,r,G,j}^{\text{loc}} = h_{R,t,G,j}^{\text{loc}} - h_{R,s,G \rightarrow G,j}^{\text{loc}}, \quad (17a)$$

$$h_{R,t,G,j}^{\text{loc}} = \int_0^1 du W_{G,j}(u) \Sigma_{\infty,t,G}^{\text{loc}}(u) \varphi_{\infty,G}^{\text{nom}}(u), \quad (17b)$$

$$h_{R,f,G}^{\text{loc}} = \int_0^1 du v \Sigma_{\infty,f,G}^{\text{loc}}(u) \varphi_{\infty,G}^{\text{nom}}(u), \quad (17c)$$

$$\begin{aligned} h_{R,s,G' \rightarrow G,j}^{\text{loc}} &= \int_0^1 du W_{G,j}(u) \\ &\times \int_0^1 du' \Sigma_{\infty,s,G' \rightarrow G}^{\text{loc}}(u' \rightarrow u) \varphi_{\infty,G'}^{\text{nom}}(u'); \end{aligned} \quad (17d)$$

- the variational rehomogenization coefficients ($h_{V,x,G,i,j}^{\text{loc}}$):

$$h_{V,r,G,i,j}^{\text{loc}} = h_{V,t,G,i,j}^{\text{loc}} - h_{V,s,G \rightarrow G,i,j}^{\text{loc}}, \quad (18a)$$

$$h_{V,t,G,i,j}^{\text{loc}} = \int_0^1 du W_{G,j}(u) \Sigma_{\infty,t,G}^{\text{loc}}(u) Q_{G,i}(u), \quad (18b)$$

$$h_{V,f,G,i}^{\text{loc}} = \int_0^1 du v \Sigma_{\infty,f,G}^{\text{loc}}(u) Q_{G,i}(u), \quad (18c)$$

$$h_{V,s,G' \rightarrow G,i,j}^{\text{loc}} = \int_0^1 du W_{G,j}(u) \int_0^1 du' \Sigma_{\infty,s,G' \rightarrow G}^{\text{loc}}(u' \rightarrow u) Q_{G',i}(u'); \quad (18d)$$

- and the fission-spectrum coefficient ($\chi_{G,j}$):

$$\chi_{G,j} = \int_0^1 du W_{G,j}(u) \chi_G(u). \quad (19)$$

The matrix of the system of Eq. (16) has rank $r = N_G N_Q^{\text{max}}$, with $N_Q^{\text{max}} = \max_{G=1, \dots, N_G} \{N_{Q_G}\}$. We build upon previous work (Gamarino et al., 2018a) to choose the basis and weighting functions $Q_{G,i}(u)$ and $W_{G,j}(u)$ for the modal synthesis of $\delta\Phi_{\infty,G}(u)$. Details about the selection of the modes are given in Section 3.1.

The few-group flux, the infinite-medium multiplication factor and the rehomogenization parameters must be known to solve Eq. (16) for the coefficients $\alpha_{\infty,G,i}$. We compute $\bar{\Phi}_{\infty,G}^{\text{loc}}$ and k_{∞}^{loc} solving the few-group, homogenized balance equation in the infinite lattice. In a two-group framework and for the practical case with fission emission only in the fast range (namely, $\chi_1 = 1$ and $\chi_2 = 0$), this can be written as

$$\begin{cases} \left(\Sigma_{a,1}^{\infty,\text{loc}} + \Sigma_{s,1 \rightarrow 2}^{\infty,\text{loc}} - \frac{1}{k_{\infty}^{\text{loc}}} v \Sigma_{f,1}^{\infty,\text{loc}} \right) \cdot \bar{\Phi}_{\infty,1}^{\text{loc}} = \left(\Sigma_{s,2 \rightarrow 1}^{\infty,\text{loc}} + \frac{1}{k_{\infty}^{\text{loc}}} v \Sigma_{f,2}^{\infty,\text{loc}} \right) \cdot \bar{\Phi}_{\infty,2}^{\text{loc}}, \\ \left(\Sigma_{a,2}^{\infty,\text{loc}} + \Sigma_{s,2 \rightarrow 1}^{\infty,\text{loc}} \right) \cdot \bar{\Phi}_{\infty,2}^{\text{loc}} = \Sigma_{s,1 \rightarrow 2}^{\infty,\text{loc}} \cdot \bar{\Phi}_{\infty,1}^{\text{loc}}. \end{cases} \quad (20)$$

From Eq. (20), the following expression is derived for the multiplication factor:

$$k_{\infty}^{\text{loc}} = \frac{v \Sigma_{f,1}^{\infty,\text{loc}}}{\Sigma_{a,1}^{\infty,\text{loc}} + \Sigma_{s,1 \rightarrow 2}^{\infty,\text{loc}}} + \frac{\Sigma_{s,1 \rightarrow 2}^{\infty,\text{loc}}}{\Sigma_{a,1}^{\infty,\text{loc}} + \Sigma_{s,1 \rightarrow 2}^{\infty,\text{loc}}} \cdot \frac{v \Sigma_{f,2}^{\infty,\text{loc}}}{\Sigma_{a,2}^{\infty,\text{loc}} + \Sigma_{s,2 \rightarrow 1}^{\infty,\text{loc}}}. \quad (21)$$

The two-group flux is computed as

$$\bar{\Phi}_{\infty,1}^{\text{loc}} = 1, \quad \bar{\Phi}_{\infty,2}^{\text{loc}} = \frac{\Sigma_{s,1 \rightarrow 2}^{\infty,\text{loc}}}{\Sigma_{a,2}^{\infty,\text{loc}} + \Sigma_{s,2 \rightarrow 1}^{\infty,\text{loc}}}. \quad (22)$$

The nodal cross sections in Eqs. (21) and (22) are determined with Eq. (5), using the value of $\delta\Sigma_{x,G}^{\infty}$ from the latest, partially converged iteration of the reconstruction procedure. In the first iteration, $\delta\Sigma_{x,G}^{\infty}$ is set to zero and only the direct effect of density variations is taken into account.

The rehomogenization parameters detailed in Eqs. (17) and (18) depend on the fine-energy macroscopic cross sections in the local conditions $[\Sigma_{\infty,x,G}^{\text{loc}}(u)]$. These can be defined as

$$\begin{aligned} \Sigma_{\infty,x,G}^{\text{loc}}(u) &= \Sigma_{\infty,x,G}^{\text{nom}}(u) + \sum_{c=1}^{n_p} \delta N_c \sigma_{\infty,x,c,G}^{\text{loc}}(u) \\ &+ \sum_{c=1}^{n_p} N_c^{\text{nom}} \delta \sigma_{\infty,x,c,G}(u), \end{aligned} \quad (23)$$

where δN_c indicates the variation in the isotopic number density between the local and nominal conditions. To a first approximation, the summations on the right-hand side of Eq. (23) are limited to the contributions of H_2O , ^{10}B and ^{135}Xe (i.e., $n_p = 3$). We temporarily neglect perturbations in the isotopic cross-section distributions (namely, the aforementioned microscopic effect), that is

$$\delta \sigma_{\infty,x,c,G}(u) \approx 0, \quad \sigma_{\infty,x,c,G}^{\text{loc}}(u) \approx \sigma_{\infty,x,c,G}^{\text{nom}}(u). \quad (24)$$

This assumption is only justified if a sufficiently fine energy mesh is used and if the variation in the state parameters is mild. In Section 2.1.2 we will show how this approximation can be relaxed.

Substituting Eqs. (23) and (24) into Eqs. (17) and (18), the rehomogenization parameters in the local conditions are estimated as

$$h_{R,x,G,j}^{\text{loc}} \approx h_{R,x,G,j}^{\text{nom}} + \sum_{c=1}^{n_p} \delta N_c h_{R,x,c,G,j}^{\text{nom}} \quad (25a)$$

and

$$h_{V,x,G,i,j}^{\text{loc}} \approx h_{V,x,G,i,j}^{\text{nom}} + \sum_{c=1}^{n_p} \delta N_c h_{V,x,c,G,i,j}^{\text{nom}} \quad (25b)$$

where we have introduced the isotopic rehomogenization coefficients $h_{R,x,c,G,j}^{\text{nom}}$ and $h_{V,x,c,G,i,j}^{\text{nom}}$:

$$h_{R,x,c,G,j}^{\text{nom}} = \int_0^1 du W_{G,j}(u) \sigma_{\infty,x,c,G}^{\text{nom}}(u) \varphi_{\infty,G}^{\text{nom}}(u), \quad (26a)$$

$$h_{V,x,c,G,i,j}^{\text{nom}} = \int_0^1 du W_{G,j}(u) \sigma_{\infty,x,c,G}^{\text{nom}}(u) Q_{G,i}(u). \quad (26b)$$

In Eq. (25), the macroscopic coefficients $h_{R,x,G,j}^{\text{nom}}$ and $h_{V,x,G,i,j}^{\text{nom}}$ are computed with Eqs. (17) and (18) using the nominal distributions $\Sigma_{\infty,x,G}^{\text{nom}}(u)$. These coefficients, and the microscopic ones detailed in Eq. (26), are to be stored as additional homogenization parameters in the cross-section libraries obtained from the subset p' (Eq. (4)). They are interpolated at p_{nom} at each cross-section update. We use (i) the ^{10}B and ^{135}Xe isotopic coefficients to update the macroscopic coefficients for absorption and removal, and (ii) the H_2O coefficients to update the macroscopic coefficients for absorption, removal, and scattering. For example, the macroscopic parameters for the removal cross section (Eqs. (17a) and (18a)) are evaluated as

$$h_{R,r,G,j}^{\text{loc}} \approx h_{R,r,G,j}^{\text{nom}} + \delta N_{\text{H}_2\text{O}} h_{R,r,\text{H}_2\text{O},G,j}^{\text{nom}} + \delta N_{\text{B}_{10}} h_{R,a,\text{B}_{10},G,j}^{\text{nom}} + \delta N_{\text{Xe}_{135}} h_{R,a,\text{Xe}_{135},G,j}^{\text{nom}} \quad (27a)$$

and

$$h_{V,r,G,i,j}^{\text{loc}} \approx h_{V,r,G,i,j}^{\text{nom}} + \delta N_{\text{H}_2\text{O}} h_{V,r,\text{H}_2\text{O},G,i,j}^{\text{nom}} + \delta N_{\text{B}_{10}} h_{V,a,\text{B}_{10},G,i,j}^{\text{nom}} + \delta N_{\text{Xe}_{135}} h_{V,a,\text{Xe}_{135},G,i,j}^{\text{nom}}. \quad (27b)$$

The rehomogenization problem of Eq. (16) is solved at each iteration of the cross-section reconstruction algorithm. Under-relaxation is performed on the coefficients $\alpha_{\infty,G,i}$ to dampen numerical oscillations in the convergence process (an under-relaxation factor $\theta = 0.5$ is used). The spectral correction on the isotopic cross section $\sigma_{x,c,G}^{\infty}$ (Eq. (12b)) is computed as

$$\delta\sigma_{x,c,G}^{\infty,s} = \frac{1}{\Phi_{\infty,G}^{\text{loc}}} \sum_{i=1}^{N_{Q_G}} \alpha_{\infty,G,i} h_{V,x,c,G,i,0}^{\text{nom}}, \quad (28)$$

where the zeroth-order coefficients $h_{V,x,c,G,i,0}^{\text{nom}}$ correspond to a unitary weighting function (i.e., $W_{G,0}(u) = 1$).

2.1.2. The microscopic effect

Deviations in the fine-group isotopic cross sections between the local and nominal conditions are mainly induced by:

- variations in the energy self-shielding properties due to changes in the moderator/coolant density;
- variations in the average fuel-to-moderator thermal-flux ratio due to perturbations in the xenon concentration.

The first contribution mostly affects resonant isotopes (such as ^{238}U) and is preminent in the fast group. The second contribution acts on the cross-section distributions of the main thermal-neutron absorbers (such as ^{235}U) and is only relevant in the thermal group.

We introduce a new type of isotopic rehomogenization coefficients to estimate the microscopic-effect and cross correction terms (Eqs. (12c) and (12d)):

$$s_{R,x,c,G,j} = \int_0^1 du W_{G,j}(u) \delta\sigma_{\infty,x,c,G}(u) \varphi_{\infty,G}^{\text{nom}}(u), \quad (29a)$$

$$s_{V,x,c,G,i,j} = \int_0^1 du W_{G,j}(u) \delta\sigma_{\infty,x,c,G}(u) Q_{G,i}(u). \quad (29b)$$

We refer to $s_{R,x,c,G,j}$ and $s_{V,x,c,G,i,j}$ as *self-shielding coefficients*. Combining Eqs. (15) and (29), Eqs. (12c) and (12d) become

$$\delta\sigma_{x,c,G}^{\infty,m} = s_{R,x,c,G,0} \quad (30a)$$

and

$$\delta\sigma_{x,c,G}^{\infty,*} = \frac{1}{\Phi_{\infty,G}^{\text{loc}}} \sum_{i=1}^{N_{Q_G}} \alpha_{\infty,G,i} s_{V,x,c,G,i,0}. \quad (30b)$$

We determine the variation functions $\delta\sigma_{\infty,x,c,G}(u)$ and the self-shielding coefficients with a heuristic approach. Below, the procedure is addressed separately for the aforementioned effects of the water density and xenon concentration.

Changes in $\rho_{\text{H}_2\text{O}}$ cause perturbations in the isotopic cross-section distributions in the epithermal region, which become significant at very low densities. In this work, we denote by epithermal the energy range between 0.625 eV and approximately 200 eV. This fraction of the energy spectrum is characterized by (i) fine-group thermalization effects at energies below about 6 eV, and (ii) self-shielding resonance absorption at energies above about 6 eV. For a UO_2 assembly with 1.8% enrichment, Fig. 1 shows the energy distribution of the homogenized, fast-group absorption cross section of ^{238}U [$\sigma_{a,1}^{238}(u)$] at the nominal conditions defined in Table 1. The fuel exposure is zero. Fig. 2 depicts the variation

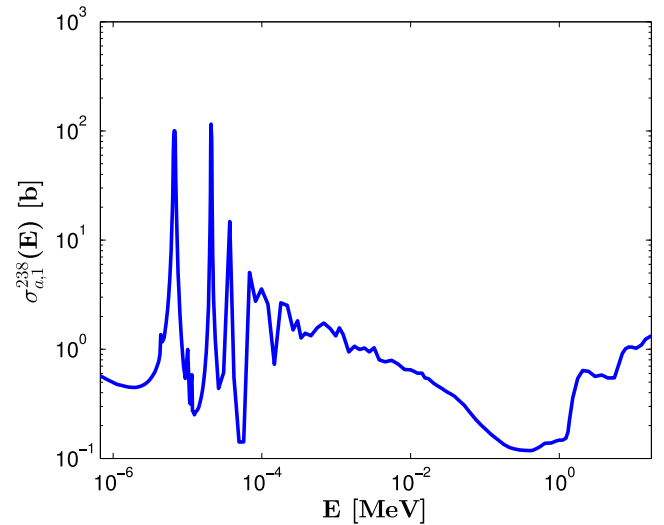


Fig. 1. Infinite-medium fine-group, homogenized absorption cross section of ^{238}U versus energy in the fast region (namely, between 0.625 eV and 19.6 MeV). The curve is computed at the nominal values of the moderator density (0.7 g/cm^3) and of the other state parameters (Table 1), and it refers to a 1.8%-enriched UO_2 assembly. Units are in barn.

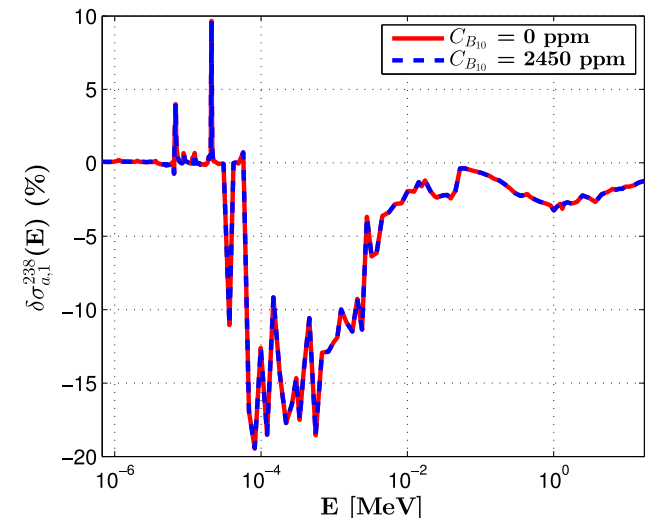


Fig. 2. Relative variation (compared to the nominal conditions of Table 1) in the fine-group, homogenized absorption cross section of ^{238}U in the fast region (depicted in Fig. 1). Local conditions correspond to $\rho_{\text{H}_2\text{O}} = 0.21 \text{ g/cm}^3$, $N_{\text{Xe}_{135}} = 0 \text{ a/\AA}^3$, $C_{\text{B}_{10}} = 0 \text{ ppm}$ (solid curve) and $C_{\text{B}_{10}} = 2450 \text{ ppm}$ (dashed curve).

in $\sigma_{a,1}^{238}(u)$ when ρ_{H_2O} is reduced to 0.21 g/cm^3 . The perturbation is displayed for two values of the soluble-boron concentration: 0 ppm and 2450 ppm. In both cases, the xenon density varies from $4.0 \cdot 10^{-9} \text{ a/\AA}^3$ to 0 a/\AA^3 . The overlap of the two curves suggests that neither the boron concentration nor the xenon density has an impact on fast-group absorption properties. The microscopic effect is thus only due to the water density. The cross-section variation in the low-lying resonance region (namely, between 6.67 eV and 208.46 eV) is apparent. An increase in absorption of 4% and 9.7% is observed for the resonances at 6.67 eV and 20.9 eV, respectively. The impact of this variation on the group-one collapsed macroscopic cross section is relevant and must be taken into account. The variation in the thermal group (not shown here) is less significant and reaches a maximum value of about 2% at 1 meV.

Since a simple relation between $\delta\sigma_{\infty,x,c,G}(u)$ and δN_{H_2O} cannot be found, we use a regression-like approach to model the dependence of self-shielding coefficients on N_{H_2O} , without cross terms involving the boron and xenon concentrations. Due to the smoothness of the corresponding behavior, one-variable polynomial approximations of order 1 to 3 proved to be sufficiently accurate. This requires to perform four additional lattice simulations for each burn-up (and, possibly, fuel-temperature) point of the cross-section libraries built in the phase space p' (Eq. (4)). For the type of fuel assembly considered in this work (i.e., UO_2 with neither control elements nor burnable absorbers), we compute the water-density self-shielding coefficients for ^{238}U , ^{235}U , and natural zirconium (Zr). These nuclides have been selected based on (i) their contribution to the fast-group macroscopic absorption and fission cross sections and (ii) the amplitude of the variation in their isotopic cross sections with water density. Plutonium isotopes must be included in depletion calculations and for MOX assembly analyses.

The contribution of changes in the xenon concentration to $\delta\sigma_{\infty,x,c,G}(u)$ is a lattice effect and can be explained as follows. In the lattice calculation, the cross section of the absorbing nuclide c (for instance, ^{235}U) in the fine energy group g is spatially homogenized over the fuel assembly as (we omit the subscript x and the superscript ∞)

$$\bar{\sigma}_{c,g} = \frac{\sum_{i_j=1}^{n_{f_c}} N_{c,i_j} \sigma_{c,g,i_j} \Phi_{g,i_j} A_{i_j}}{\bar{N}_c \bar{\Phi}_g A_{fa}}, \quad (31)$$

where n_{f_c} is the number of fuel cells in the assembly, A_{i_j} is the cross-sectional area of the i_j -th cell, A_{fa} is the cross-sectional area of the whole assembly, \bar{N}_c is the assembly-averaged number density, and $\bar{\Phi}_g$ is the g^{th} -group assembly-averaged flux (with the water tubes and the water gap included in the smearing). The quantities N_{c,i_j} and σ_{c,g,i_j} are invariant to the physical conditions in the node. If the level of xenon increases (or decreases) compared to its nominal value, the thermal flux becomes more (or less) depressed in the fuel rods. This causes an increase (or decrease) in the ratio of the average flux in the moderator to that in the fuel, commonly referred to as *thermal disadvantage factor* (Duderstadt and Hamilton, 1976). Hence, the ratio $\Phi_{g,i_j}/\bar{\Phi}_g$ in Eq. (31) decreases (or increases), and so does $\bar{\sigma}_{c,g}$. This change is less relevant when considering fuel assemblies without empty guide tubes, empty instrumentation tubes, and water channels in general. The correction term for such xenon-induced effect is also computed with a heuristic approach, based on the following observations for the variation function $\delta\sigma_{\infty,x,c,G}(u)$ within the thermal coarse group:

- for a given $\delta N_{Xe_{135}}$, the dependence of the variation function on the other state parameters is negligible (for $C_{B_{10}}$) or small (for ρ_{H_2O});

- the shape of the variation function does not vary with $\delta N_{Xe_{135}}$;
- the magnitude of the variation function scales linearly with $\delta N_{Xe_{135}}$.

The first property is apparent in Fig. 3, which shows the behavior of the thermal-absorption variation function of ^{235}U in the 1.8%-enriched UO_2 assembly considered before. The variation has been computed at $N_{Xe_{135}} = 0 \text{ a/\AA}^3$. Three curves are displayed, corresponding to different values of N_{H_2O} and $N_{B_{10}}$. The second and third properties can be observed in Fig. 4, which depicts the same variation function for different values of $N_{Xe_{135}}$ at $\rho_{H_2O}^{\text{nom}}$ and $C_{B_{10}}^{\text{nom}}$. The solid marked lines correspond to the reference distributions $\delta\sigma_{\infty,x,c,G}^{\text{ref}}(u)$, whereas the dashed lines correspond to the distributions computed with the following approximate relation of linearity:

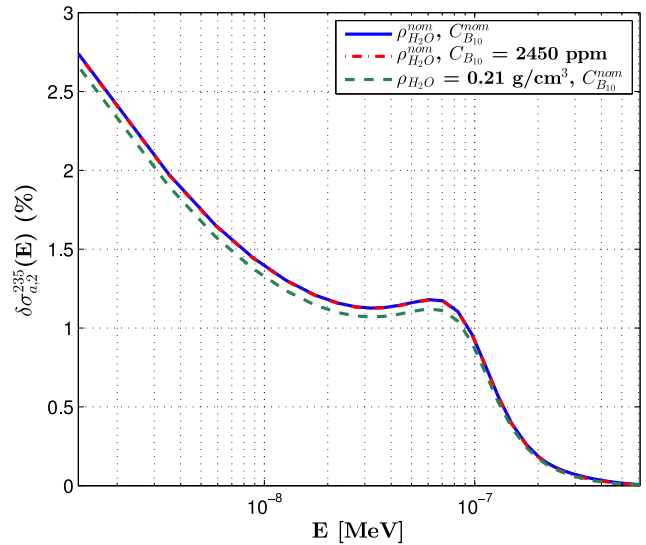


Fig. 3. Relative variation (compared to the nominal conditions of Table 1) in the infinite-medium fine-group, homogenized absorption cross section of ^{235}U in the thermal region. The local conditions correspond to $N_{Xe_{135}} = 0 \text{ a/\AA}^3$ and different combinations of ρ_{H_2O} and $C_{B_{10}}$.

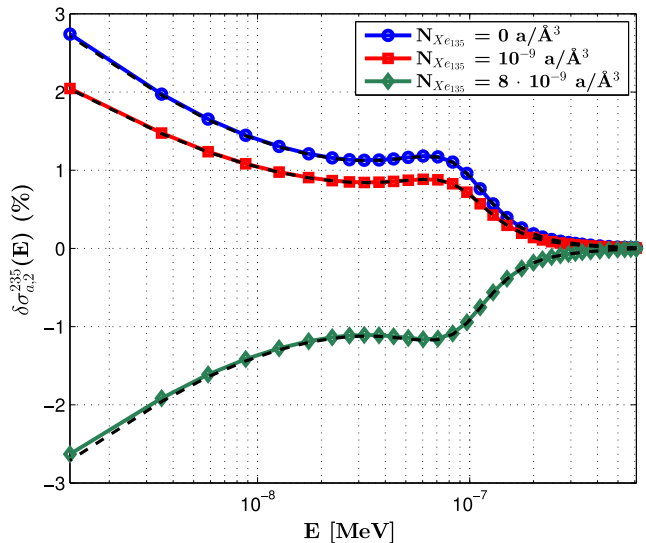


Fig. 4. Impact of $N_{Xe_{135}}$ on the variation in the infinite-medium fine-group, homogenized absorption cross section of ^{235}U in the thermal region. The values of ρ_{H_2O} and $C_{B_{10}}$ are the nominal ones (Table 1). The dashed curves have been computed using a linear approximation (Eq. (32)).

$$\delta\sigma_{\infty,x,c,G}(u) \approx \left(\sigma_{\infty,x,c,G}^{\text{sample}}(u) - \sigma_{\infty,x,c,G}^{\text{nom}}(u) \right) \frac{\delta N_{Xe135}}{\delta N_{Xe135}^{\text{sample}}}. \quad (32)$$

In Eq. (32), $\sigma_{\infty,x,c,G}^{\text{sample}}(u)$ is the reference distribution evaluated at a sample concentration of xenon ($N_{Xe135}^{\text{sample}} = 2.0 \cdot 10^{-9} \text{ a/\AA}^3$ in the example of Fig. 4) and at the nominal values of ρ_{H_2O} and C_{B10} . We have $\delta N_{Xe135}^{\text{sample}} = N_{Xe135}^{\text{sample}} - N_{Xe135}^{\text{nom}}$. Clearly, Eq. (32) provides a very accurate estimate of the reference variation. It can thus be used to model the dependence of the coefficients $s_{R,x,c,G,j}$ and $s_{V,x,c,G,i,j}$ (Eq. (29)) on N_{Xe135} . This approach only requires, for each value of the burn-up, the simulation of an additional state during the lattice calculation to obtain the sample distribution $\sigma_{\infty,x,c,G}^{\text{sample}}(u)$. In the on-line calculation, the local coefficients are estimated as

$$s_{R,x,c,G,j} \approx s_{R,x,c,G,j}^{\text{sample}} \frac{\delta N_{Xe135}}{\delta N_{Xe135}^{\text{sample}}}, \quad s_{V,x,c,G,i,j} \approx s_{V,x,c,G,i,j}^{\text{sample}} \frac{\delta N_{Xe135}}{\delta N_{Xe135}^{\text{sample}}}. \quad (33)$$

In the analysis presented in this work, we compute the xenon-related correction terms of Eq. (30) for the thermal absorption in ^{235}U , ^{135}Xe , ^{10}B and H_2O , and for the thermal fission in ^{235}U . As it will be shown in Section 3, the spectrum variation $\delta\Phi_{\infty,2}(u)$ is zero at very low energies (i.e., below approximately 3 meV), where the variation function has the highest magnitude. It follows that the cross correction $\delta\sigma_{x,c,G}^{\infty,*}$ is considerably smaller than the microscopic one $\delta\sigma_{x,c,G}^{\infty,m}$.

It should be noted that a lattice effect similar to that observed for xenon also occurs when the soluble-boron concentration changes. However, the corresponding variation in the fine-group cross sections is less relevant. For instance, the change in the thermal absorption of ^{235}U at 2450 ppm has a maximum value of about 0.15% at 1 meV. Since the corresponding impact on the collapsed thermal cross sections is negligible, this kind of correction is not applied for perturbations in C_{B10} .

As explained in Section 2.1.1, before solving the spectral rehomogenization problem (Eq. (16)) the direct effect of nuclide density changes is incorporated into the standard macroscopic rehomogenization coefficients $h_{R,x,c,G,j}^{\text{nom}}$ and $h_{V,x,c,G,i,j}^{\text{nom}}$ with Eq. (25). Using the self-shielding coefficients of Eq. (29), we introduce an additional cor-

rection to include the microscopic effects in the reconstruction of the spectrum deformation. For example, Eq. (25b) becomes

$$h_{V,x,c,G,i,j}^{\text{loc}} \approx h_{V,x,c,G,i,j}^{\text{nom}} + \sum_{c=1}^{n_p} \delta N_c \left(h_{V,x,c,G,i,j}^{\text{nom}} + s_{V,x,c,G,i,j} \right) + \sum_{q=1}^{n_s} N_q^{\text{loc}} s_{V,x,q,G,i,j}, \quad (34)$$

where the index q cycles over the aforementioned relevant isotopes other than ^{10}B , ^{135}Xe , and H_2O (namely, ^{238}U , ^{235}U , and Zr for the water-density self-shielding effect; ^{235}U for the xenon-variation effect). For burnable nuclides, the atomic density N_q^{loc} comes from the environmental depletion calculation in the local conditions. We have verified that only the xenon-variation component of this correction has an impact on the solution of Eq. (16). The accuracy of the computed spectrum perturbation does not vary if we neglect the water-density microscopic effect on the macroscopic $h_{R,x,c,G,j}^{\text{loc}}$ and $h_{V,x,c,G,i,j}^{\text{loc}}$ coefficients (namely, if Eq. (25) is used instead of Eq. (34)), even at very low values of ρ_{H_2O} . Hence, the high-order (i.e., with $j > 0$) $s_{R,x,c,G,j}$ and $s_{V,x,c,G,i,j}$ coefficients are only computed for the xenon-induced microscopic effect. This allows us to minimize the regression cost for the calculation of water-density self-shielding coefficients.

2.1.3. Overview

At each iteration step, the global isotopic cross-section correction is computed summing the contributions of Eqs. (28) and (30):

$$\delta\sigma_{x,c,G}^{\infty} = s_{R,x,c,G,0} + \frac{1}{\Phi_{\infty,G}^{\text{loc}}} \sum_{i=1}^{N_{Q_G}} \alpha_{\infty,G,i} \left(h_{V,x,c,G,i,0}^{\text{nom}} + s_{V,x,c,G,i,0} \right). \quad (35)$$

The global macroscopic correction is determined as

$$\delta\Sigma_{x,G}^{\infty} = \frac{1}{\Phi_{\infty,G}^{\text{loc}}} \sum_{i=1}^{N_{Q_G}} \alpha_{\infty,G,i} h_{V,x,c,G,i,0}^{\text{loc}}, \quad (36)$$

with the coefficients $h_{V,x,c,G,i,0}^{\text{loc}}$ defined according to Eq. (34). A similar expression holds for the correction of the diffusion coefficient δD_G^{∞} . Some considerations about its calculation are made in Section 4.3.

A flow diagram of the local cross-section reconstruction algorithm is depicted in Fig. 5. At the beginning of a new burn-up step

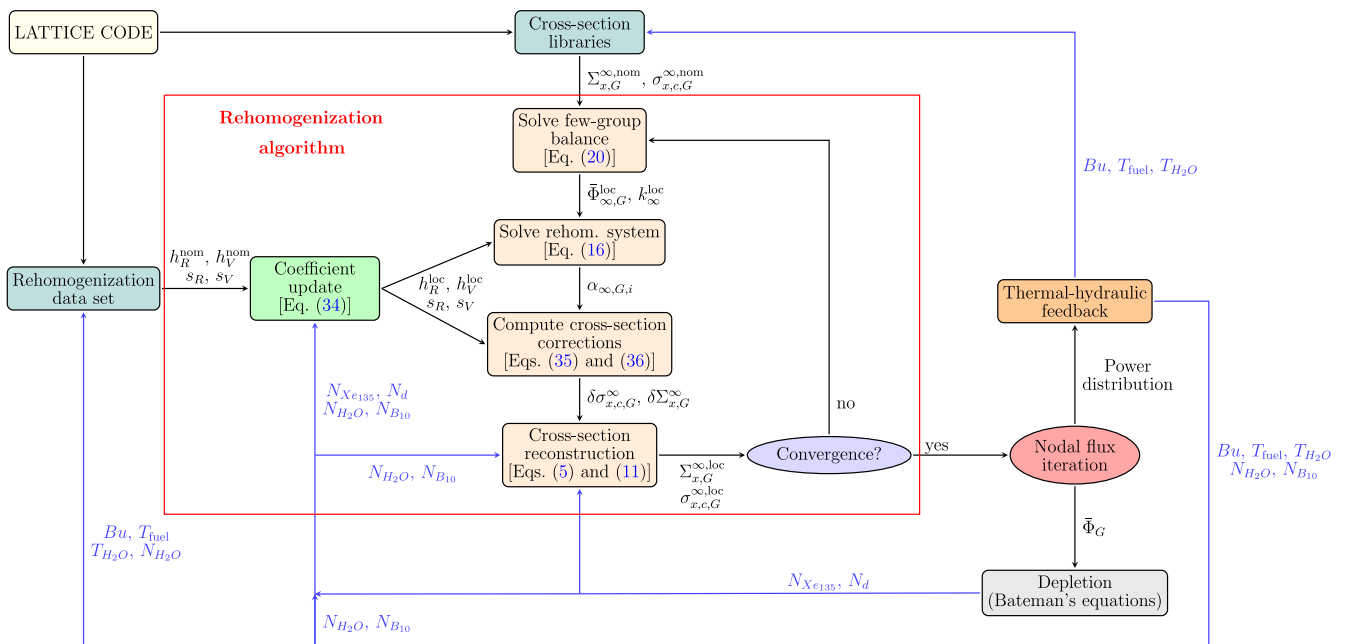


Fig. 5. Flow diagram of the rehomogenization-based algorithm for the reconstruction of the infinite-medium cross sections in a given node. The blue arrows represent the flow of state-parameter information (N_d denotes the number densities of the most relevant isotopes tracked in the fuel depletion calculation).

or after a thermal-hydraulic update, the few-group cross sections and the rehomogenization coefficients are evaluated at the new values of Bu , T_{fuel} and $T_{\text{H}_2\text{O}}$ in a given node and at the nominal values of $\rho_{\text{H}_2\text{O}}$, $C_{\text{B}_{10}}$ and $N_{\text{Xe}_{135}}$. The rehomogenization problem (Eq. (16)) is solved using (i) the values of $\bar{\Phi}_{\infty,G}^{\text{loc}}$ and k_{∞}^{loc} ensuing from the few-group infinite-medium balance (Eq. (20)), and (ii) the rehomogenization coefficients updated via Eq. (34) to account for the direct and microscopic effects of variations in $\rho_{\text{H}_2\text{O}}$, $C_{\text{B}_{10}}$, and $N_{\text{Xe}_{135}}$. The isotopic and macroscopic cross-section corrections are computed with Eqs. (35) and (36). The cross-section reconstruction follows with Eqs. (5) and (11). This procedure is repeated until convergence of $\bar{\Phi}_{\infty,G}^{\text{loc}}$ and k_{∞}^{loc} , upon which the so obtained cross sections can be used in the core nodal calculation. Homogenized cross sections are reconstructed independently in each node of the computational domain. Therefore, the algorithm can be easily parallelized.

It is remarked that during the lattice depletion calculation only the water density and the boron concentration are kept at their nominal values. The xenon density is set to the equilibrium value computed with the infinite-medium flux of the transport calculation at a given burn-up step, as it is commonly done in lattice codes. The nominal value $N_{\text{Xe}_{135}}^{\text{nom}}$ is only used when the cross-section tables are built.

2.2. Incorporation of neighbor effects

When a fuel assembly is simulated within the reactor core, the spectral effects of local nuclide density changes and interassembly neutron streaming cannot be separated. We now seek the spectrum deformation resulting from these combination of the two effects.

We compute the variation $\delta\Phi_G(u)$ between the real environment in the local physical conditions and the infinite lattice in the nominal conditions. Eq. (9) becomes

$$\Phi_{\text{env},G}^{\text{loc}}(u) = \bar{\Phi}_G \varphi_{\infty,G}^{\text{nom}}(u) + \delta\Phi_G(u), \quad (37)$$

where the few-group environmental flux $\bar{\Phi}_G$ (we have dropped the superscript *loc*) is now taken from the latest power iteration of the nodal calculation. The spectral rehomogenization problem (Eq. (16)) is rewritten replacing k_{∞}^{loc} with the core effective multiplication factor k_{eff} (which also comes from the previous nodal iteration) and adding the internodal-leakage term (Gamarino et al., 2018a,b):

$$\begin{aligned} \bar{\Phi}_G h_{R,r,G,j}^{\text{loc}} + \sum_{i=1}^{N_{Q_G}} \alpha_{G,i} h_{V,r,G,i,j}^{\text{loc}} + \bar{L}_G h_{L,G,j}^{\text{loc}} \\ = \frac{\chi_{G,j}}{k_{\text{eff}}} \sum_{G'=1}^{N_G} \left(\bar{\Phi}_{G'} h_{R,f,G'}^{\text{loc}} + \sum_{i=1}^{N_{Q_{G'}}} \alpha_{G',i} h_{V,f,G',i}^{\text{loc}} \right) \\ + \sum_{\substack{G'=1 \\ G' \neq G}}^{N_G} \left(\bar{\Phi}_{G'} h_{R,S,G'-G,j}^{\text{loc}} + \sum_{i=1}^{N_{Q_{G'}}} \alpha_{G',i} h_{V,S,G'-G,i,j}^{\text{loc}} \right), \end{aligned} \quad (38)$$

where \bar{L}_G is the few-group, node-averaged leakage from the latest flux iteration. The leakage projection coefficient $h_{L,G,j}^{\text{loc}}$ is defined as

$$h_{L,G,j}^{\text{loc}} = \int_0^1 du W_{G,j}(u) f_{L,G}^{\text{loc}}(u), \quad (39)$$

where $f_{L,G}^{\text{loc}}(u)$ denotes the spectral distribution of the environmental neutron leakage. Fick's diffusion law is applied to approximate this function at the interfaces between the generic node k and its N_{nb} neighbors m (Gamarino et al., 2018b). Under the assumption that the diffusion-coefficient energy distribution does not vary signifi-

cantly in bordering nodes, the following expression for $h_{L,G,j}^{\text{loc}}$ is obtained:

$$\begin{aligned} h_{L,G,j}^{\text{loc}} \approx \sum_{m=1}^{N_{nb}} b_G^{k,m} \left[\left(\bar{\Phi}_G^k h_{R,D,G,j}^{\text{loc}} + \sum_{i=1}^{N_{Q_G}} \alpha_{G,i}^k h_{V,D,G,i,j}^{\text{loc}} \right) \right. \\ \left. - \left(\bar{\Phi}_G^m h_{R,D,G,j}^{\text{loc}} + \sum_{i=1}^{N_{Q_G}} \alpha_{G,i}^m h_{V,D,G,i,j}^{\text{loc}} \right) \right], \end{aligned} \quad (40)$$

where $b_G^{k,m}$ is a normalization constant (scaling the group- G integral leakage to \bar{L}_G), and $h_{R,D,G,j}^{\text{loc}}$ and $h_{V,D,G,i,j}^{\text{loc}}$ are the local rehomogenization parameters for the diffusion coefficient (see Section 4.3 for details about their calculation from the nominal counterparts $h_{R,D,G,j}^{\text{nom}}$ and $h_{V,D,G,i,j}^{\text{nom}}$). The non-linearity of this diffusive strategy is resolved computing $h_{L,G,j}^{\text{loc}}$ with the coefficients $\alpha_{G,i}$ from the previous rehomogenization iteration.

The microscopic and macroscopic cross-section corrections are determined with Eqs. (35) and (36), using the core-environment coefficients $\alpha_{G,i}$ and the rehomogenization parameters ensuing from Eqs. (26), (29), and (34). The environmental effects on the rehomogenization coefficients (i.e., on the fine-energy cross sections) are neglected. In Gamarino et al. (2018a) we showed that the error introduced with this approximation is negligible.

Fig. 6 illustrates how the rehomogenization algorithm is nested in the core simulation when the environmental effects are incorporated into the cross-section reconstruction. Compared to the infinite-medium reconstruction, multiple iterations after the interpolation at p_{nom} (see Fig. 5) are not necessary. The method can thus be viewed as an additional feedback in the coupling between the nodal flux solver and the thermal-hydraulic and depletion modules.

3. Numerical results

In this section we apply the proposed method to several test cases. A two-group energy structure is chosen for the nodal cross sections. We first focus on the reconstruction of the local infinite-medium cross sections of a standard UO_2 fuel assembly (Section 3.1). Afterwards, we investigate a multiassembly benchmark problem with significant spectral effects due to internodal heterogeneity (Section 3.2). In this example, we test the reconstruction of cross sections in the real environment at the local conditions.

3.1. Reconstruction of the single-assembly cross sections

We consider a 17×17 UO_2 fuel assembly with 1.8% enrichment. The fuel bundle contains twenty-four empty guide tubes and an empty instrumentation tube, which are made of a Zircaloy-4 alloy. The assembly side has size 21.61 cm, with the cell pitch and the water gap measuring 1.26 cm and 0.8 mm, respectively. The assembly layout is depicted in Fig. 7. The cross-section reconstruction algorithm as described in Section 2.1 has been implemented in the BRISINGR nodal diffusion code (Gamarino et al., 2018b). In the analysis that follows, infinite-lattice calculations for the generation of two-group cross sections in the nominal conditions are performed with the APOLLO2-A deterministic transport code (Martinoli et al., 2010). The critical-buckling correction is not applied ($B^2 = 0$). A 281-group discretization is used for the neutron spectrum and the fine-energy cross-section distributions. We consider 247 groups in the fast region and 34 groups in the thermal one, with the following energy boundaries (Eq. (8)): $E_1^+ = 19.6$ MeV, $E_1^- \equiv E_2^+ = 0.625$ eV (thermal cut-off), and $E_2^- = 0.11$ meV.

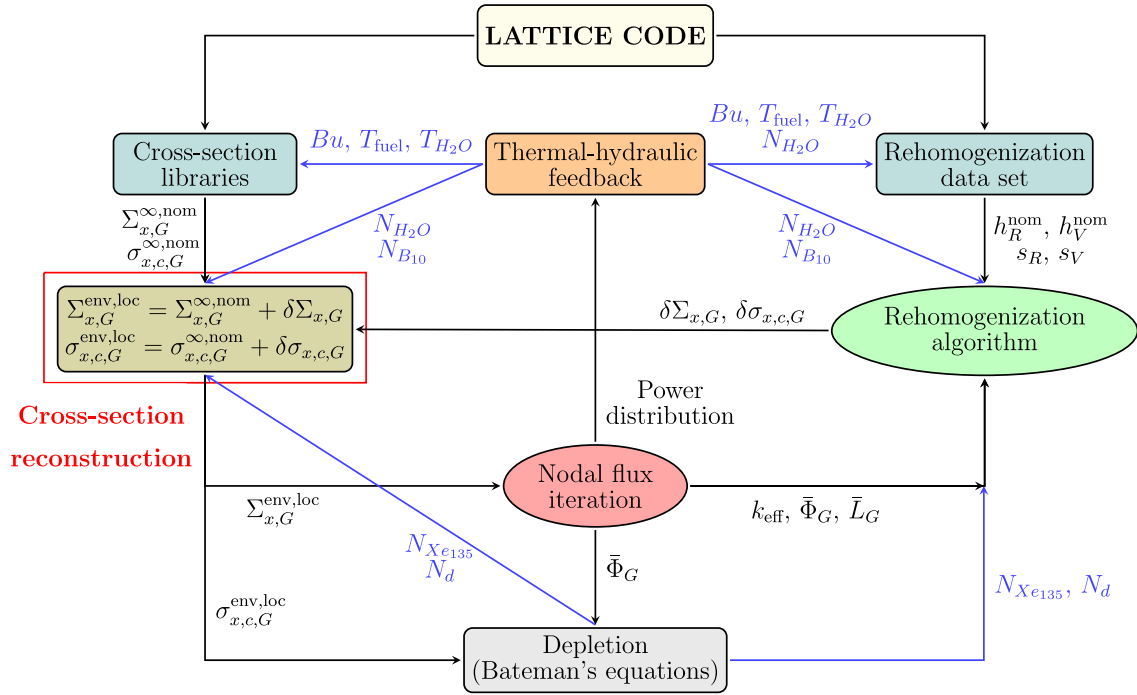


Fig. 6. Flow diagram of the core calculation when the nodal cross sections are directly reconstructed in the real environment at the local conditions.

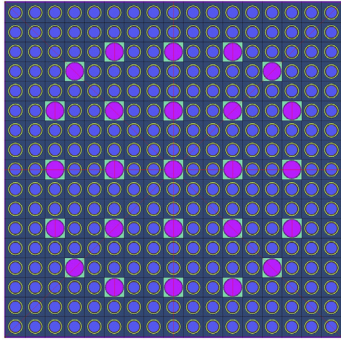


Fig. 7. Internal layout of the 1.8%-enriched UO_2 fuel assembly considered in the analysis.

The spectrum-variation basis functions $Q_{G,i}(u)$ (Eq. (15)) are determined with the Proper Orthogonal Decomposition (POD) approach described in Gamarino et al. (2018a). The POD modes are extracted from the Singular Value Decomposition (SVD) of a set of snapshots of the reference spectrum perturbation. The snapshots have been computed sampling the whole range of the values of $\rho_{\text{H}_2\text{O}}$, $C_{\text{B}_{10}}$ and $N_{\text{Xe}_{135}}$ that can be encountered in a reactor core. We have used 100 snapshots for the basis calculation. In both coarse energy groups, the spectrum perturbation is synthesized with the first four modes ensuing from this procedure. These are shown in Fig. 8. With this choice, the rank of the rehomogenization matrix (Eq. (16)) is 8. The rehomogenization coefficients (Eqs. (17)–(19), (26), and (29)) are computed based on Galerkin projection of Eq. (13) (namely, the weighting functions $W_{G,j}(u)$ are chosen to be equal to the basis functions).

The single-assembly cross sections are generated at zero burn-up and at the nominal values of $\rho_{\text{H}_2\text{O}}$, $C_{\text{B}_{10}}$ and $N_{\text{Xe}_{135}}$ defined in Table 1. Since we simulate fresh-fuel conditions, in all test cases the local xenon density is set to $0 \text{ a}/\text{\AA}^3$, which corresponds to a

strong variation from its nominal value of $4.0 \cdot 10^{-9} \text{ a}/\text{\AA}^3$ as seen in Section 2.1. In some of the examples shown in this section, the nominal value of the xenon level is also set to $0 \text{ a}/\text{\AA}^3$. This is solely done to allow standalone (i.e., single-parameter) variations in the moderator density and in the boron concentration. In this way, one can assess the accuracy of the cross-section reconstruction individually (namely, without the influence of xenon) for each of these two variables. We consider variations in the boron concentration within the range [0 ppm, 3200 ppm]. The water density is spanned in the interval [$0.21 \text{ g}/\text{cm}^3$, $1.0 \text{ g}/\text{cm}^3$]. In order to keep the analysis unaffected by interpolation errors, we compute the nominal cross sections at the exact values of the fuel and moderator temperatures. When simulating normal operating conditions, we set $T_{\text{fuel}} = 851.5 \text{ K}$ and $T_{\text{H}_2\text{O}} = 586.1 \text{ K}$.

The macroscopic and microscopic cross sections predicted with the rehomogenization-based algorithm ($\Sigma_{x,G}^{\text{loc}}$, $\sigma_{x,c,G}^{\text{loc}}$) are compared to those obtained in APOLLO2-A at the exact, local conditions ($\Sigma_{x,G}^{\text{loc,ref}}$, $\sigma_{x,c,G}^{\text{loc,ref}}$). The errors in the reconstructed cross sections are computed as

$$\Delta \Sigma_{x,G}^{\infty} = \frac{\Sigma_{x,G}^{\text{loc}} - \Sigma_{x,G}^{\text{loc,ref}}}{\Sigma_{x,G}^{\text{loc,ref}}} \cdot 100\%,$$

$$\Delta \sigma_{x,c,G}^{\infty} = \frac{\sigma_{x,c,G}^{\text{loc}} - \sigma_{x,c,G}^{\text{loc,ref}}}{\sigma_{x,c,G}^{\text{loc,ref}}} \cdot 100\%. \quad (41)$$

The variation in the macroscopic cross sections between the local and nominal conditions is determined as

$$\delta \Sigma_{x,G}^{\infty} = \frac{\Sigma_{x,G}^{\text{loc}} - \Sigma_{x,G}^{\text{nom}}}{\Sigma_{x,G}^{\text{nom}}} \cdot 100\%. \quad (42)$$

Similar expressions hold for the errors and variations in the multiplication factor (Δk_{∞} , δk_{∞}), in the two-group node-averaged flux ($\Delta \bar{\Phi}_{\infty,G}$, $\delta \bar{\Phi}_{\infty,G}$), and in the node-averaged total fission power ($\Delta \bar{P}_{\text{fiss}}^{\infty}$, $\delta \bar{P}_{\text{fiss}}^{\infty}$).

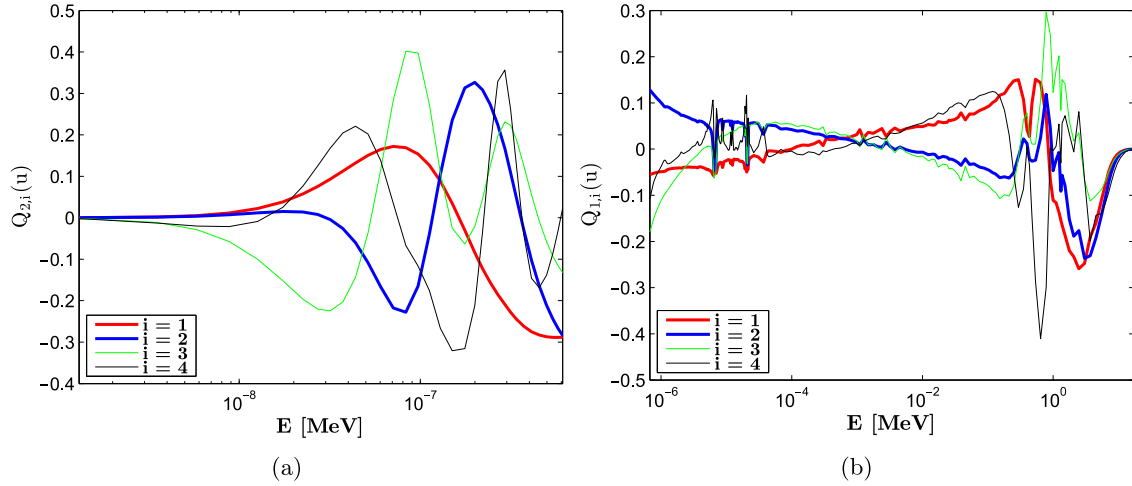


Fig. 8. (a) Thermal-group and (b) fast-group POD basis functions computed with the method of snapshots and the SVD.

Our target in terms of accuracy is to have:

- errors not exceeding 50 pcm in k_{∞} and 0.1% in the macroscopic cross sections in frequent conditions (namely, in the normal range of operation);
- errors not exceeding 100 pcm in k_{∞} and 0.5% in the macroscopic cross sections in abnormal operating points (such as very low moderator densities) that are typically reached in accidental conditions.

We include in the second category the transitions from cold to hot conditions during the reactor start-up and from hot to cold conditions when the reactor is shut down. We believe that the above error bounds are reasonably low considered the range of accuracy of nodal diffusion tools. For instance, the values chosen for normal operating conditions would be easily concealed by homogenization errors arising in heterogeneous core configurations.

The convergence of the reconstruction algorithm (Fig. 5) is reached when the relative changes in k_{∞}^{loc} and in the nodal flux two-norm between two successive iterations drop below a tolerance $\epsilon_{\text{iter}} = 10^{-5}$.

The analysis is structured as follows. We first present sample results for variations in only one parameter (or two, depending on the nominal value set for the xenon concentration as explained above). Afterwards, simultaneous perturbations in the three parameters are addressed.

3.1.1. Variation in the xenon concentration

We consider a perturbed configuration with $N_{\text{Xe}_{135}}^{\text{loc}} = 0 \text{ a}/\text{\AA}^3$ and $\delta N_{\text{Xe}_{135}} = -4 \cdot 10^{-9} \text{ a}/\text{\AA}^3$. The boron concentration and the water density are at their nominal values. The reference value of k_{∞}^{loc} is 1.08277.

Fig. 9 shows the thermal-group spectrum variation (per unit pseudo lethargy) due to this perturbation. The deformation in the fast group is negligible (its magnitude ranges from -0.01% to 0.05%) and is therefore not shown. The reference change is very accurately predicted by the method. Table 2 reports the errors in the computed macroscopic cross sections and in the main integral parameters. The two flux-error values refer to the fast and thermal groups. The number of iterations (n_{iter}) of the reconstruction algorithm is also shown. The deviations are negligible for all quantities. If the xenon-variation microscopic effect (Section 2.1.2) is not taken into account, the errors in $\Sigma_{a,2}^{\infty}$ and $\nu\Sigma_{f,2}^{\infty}$ increase to

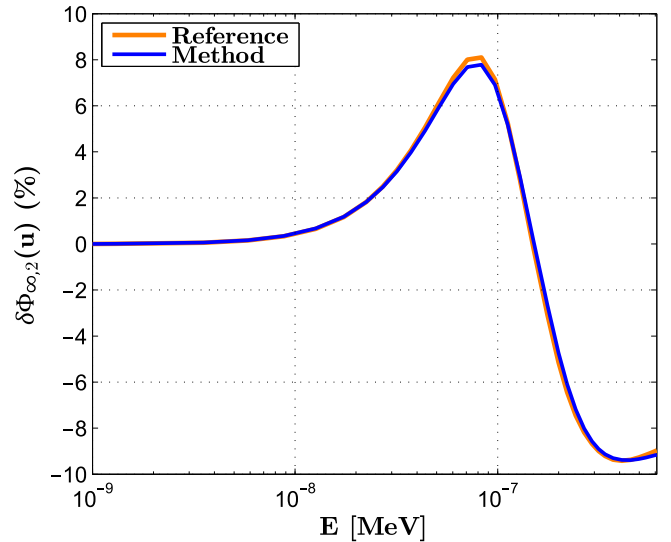


Fig. 9. Thermal-group spectrum variation (per unit u) versus energy due to a change in $N_{\text{Xe}_{135}}$ from $4.0 \cdot 10^{-9} \text{ a}/\text{\AA}^3$ to $0 \text{ a}/\text{\AA}^3$. The values of the moderator density and boron concentration are the nominal ones (Table 1).

-0.55% and -0.82% , respectively, and the error in k_{∞} becomes -249 pcm .

The interplay among the various effects (direct, spectral, and microscopic) of the xenon perturbation is quantified in Table 3, which shows the corresponding contributions to the reference global variation in the cross sections and integral parameters. For this kind of perturbation, the spectral and microscopic effects play a secondary role compared to the direct one.

3.1.2. Variations in the concentration of diluted boron

We analyze two examples with varying concentration of diluted boron:

- a transition from 700 ppm to 2450 ppm, with $N_{\text{Xe}_{135}} = 0 \text{ a}/\text{\AA}^3$ in both nominal and perturbed conditions (case a);
- a transition from 700 ppm to 0 ppm, with $N_{\text{Xe}_{135}} = 4.0 \cdot 10^{-9} \text{ a}/\text{\AA}^3$ in the nominal state and $N_{\text{Xe}_{135}} = 0 \text{ a}/\text{\AA}^3$ in the perturbed one (case b).

In case a, the boron concentration is the only varying parameter. The first perturbed value of $C_{B_{10}}$ (2450 ppm) may be representative

Table 2Transition from $N_{Xe_{135}} = 4.0 \cdot 10^{-9} \text{ a}/\text{\AA}^3$ to $N_{Xe_{135}} = 0 \text{ a}/\text{\AA}^3$: errors in the reconstructed macroscopic cross sections and in the main integral parameters, and number of iterations.

$\Delta\Sigma_{a,1}^{\infty}$ (%)	$\Delta\Sigma_{a,2}^{\infty}$ (%)	$\Delta\nu\Sigma_{f,1}^{\infty}$ (%)	$\Delta\nu\Sigma_{f,2}^{\infty}$ (%)	$\Delta\Sigma_{s,1 \rightarrow 2}^{\infty}$ (%)	Δk_{∞} [pcm]	$\Delta\Phi_{\infty,G}$ (%)	$\Delta\bar{P}_{\text{fiss}}^{\infty}$ (%)	n_{iter}
0.011	0.003	-0.009	0.008	0.01	-2	-0.002, 0.006	0.01	7

Table 3Variation in the macroscopic cross sections and integral parameters due to a change in $N_{Xe_{135}}$ from $4.0 \cdot 10^{-9} \text{ a}/\text{\AA}^3$ to $0 \text{ a}/\text{\AA}^3$. The global variation and its spectral and microscopic components have been determined with the reference data from APOLLO2-A. The reference perturbed cross sections are $\Sigma_{a,2}^{\infty} = 0.066702 \text{ cm}^{-1}$ and $\nu\Sigma_{f,2}^{\infty} = 0.080904 \text{ cm}^{-1}$.

	$\delta\Sigma_{a,2}^{\infty}$ (%)	$\delta\nu\Sigma_{f,2}^{\infty}$ (%)	δk_{∞} [pcm]	$\delta\Phi_{\infty,G}$ (%)	$\delta\bar{P}_{\text{fiss}}^{\infty}$ (%)
Direct	-8.94	0.0	7930	-1.92, 7.50	5.81
Spectr. + micr. (Ref.)	1.49	1.95	311	0.31, -1.2	0.77
Global (Ref.)	-7.44	1.95	8241	-1.62, 6.3	6.58

of the beginning of the core life at hot full-power conditions in the absence of burnable poison and with all control rods out. The second value (0 ppm) is typically found at the end of a fuel cycle. The reference values of k_{∞} in the two perturbed conditions are 0.87077 (case *a*) and 1.20541 (case *b*). In case *a*, in which there is neither xenon nor water-density variation, the microscopic effect is not taken into account (namely, the corrections of Eqs. (12c) and (12d) are neglected).

Fig. 10 depicts the spectrum perturbations in the two test cases. The deformation is significant in the thermal group, whereas the fast group is only affected in the epithermal range. The result of the calculation is flawless in the thermal and epithermal regions. The deviations from the reference found at high energies (especially at $E > 100 \text{ keV}$ in case *b*) have negligible impact on the reconstruction of the fast-group cross sections, because in this range the magnitude of $\delta\Phi_{\infty,1}(u)$ is low and only the fission cross sections are relatively high, due to the contribution of fast fissions of ^{238}U . The errors in the macroscopic cross sections and integral parameters are in Table 4. Table 5 shows the errors in the rehomogenized isotopic cross sections of some relevant nuclides. We have observed that the deviations have the same order of magnitude as the errors found with the conventional multivariate interpolation. For case *a*, Table 6 reports the contributions of the various effects to the overall variation in the macroscopic cross sections and in the integral parameters. Also in this case, the direct effect is preeminent.

We have made a parametric analysis by considering the whole range of variation of the boric-acid concentration in a reactor core. Fig. 11 shows the errors in k_{∞} and in the node-averaged total fission power versus the boron concentration. The zero-error bar is highlighted. The errors in the macroscopic thermal absorption and production cross sections are plotted in Fig. 12. The results are shown for the cases with $N_{Xe_{135}}^{\text{nom}} = 0 \text{ a}/\text{\AA}^3$ and $N_{Xe_{135}}^{\text{nom}} = 4.0 \cdot 10^{-9} \text{ a}/\text{\AA}^3$. In the former (i.e., when $C_{B_{10}}$ is the only changing parameter), the deviations are negligible along the whole boron axis. In the latter (i.e., with a combined variation of the two variables), their magnitude is somewhat higher, yet remains within the target bounds (50 pcm for k_{∞} , 0.1% for the macroscopic cross sections). Only at 3200 ppm, the errors in k_{∞} and $\nu\Sigma_{f,2}^{\infty}$ (-45 pcm and -0.11%, respectively) are close to or slightly exceed the prescribed limits. However, values of $C_{B_{10}}$ higher than 3000 ppm are uncommon in modern PWR core design. The amount of chemical shim is limited (usually to 2000 or 2500 ppm) to avoid a positive moderator void coefficient of reactivity (Duderstadt and Hamilton, 1976).

3.1.3. Variations in the water density

Following the same approach as for the boron concentration, we consider three examples with perturbations in the moderator density:

- a transition from 0.7 g/cm^3 to 0.76 g/cm^3 , with $N_{Xe_{135}}^{\text{nom}} = 4.0 \cdot 10^{-9} \text{ a}/\text{\AA}^3$ and $N_{Xe_{135}}^{\text{loc}} = 0 \text{ a}/\text{\AA}^3$ (case *a*);
- a transition from 0.7 g/cm^3 to 0.91 g/cm^3 , with $N_{Xe_{135}}^{\text{nom}} = 4.0 \cdot 10^{-9} \text{ a}/\text{\AA}^3$ and $N_{Xe_{135}}^{\text{loc}} = 0 \text{ a}/\text{\AA}^3$ (case *b*);
- a transition from 0.7 g/cm^3 to 0.21 g/cm^3 , with $N_{Xe_{135}} = 0 \text{ a}/\text{\AA}^3$ in both nominal and perturbed conditions (case *c*).

Case *a* is an example of mild fluctuation during normal operation. It corresponds to a change in the moderator temperature of about 30 K at the nominal pressure (158 bar). Cases *b* and *c* are instead examples of strong perturbations. The first value of ρ_{H_2O} (0.91 g/cm^3) is encountered in the transition from cold zero power to hot full power during the reactor start-up. The second value (0.21 g/cm^3) may occur in design basis accidents, such as loss-of-flow accidents. The reference values of k_{∞} in the three perturbed states are 1.08028 (case *a*), 1.06777 (case *b*), and 0.93046 (case *c*).

Fig. 13 shows the spectrum perturbations of cases *b* and *c*. Compared to the previous examples, a significant deformation also takes place in the fast group. At $\rho_{H_2O} = 0.21 \text{ g/cm}^3$, the magnitude of the perturbation becomes remarkable along the whole energy axis. The shape of the variation features a double peak in the range 50 keV - 19.6 MeV, which changes sign at about 1 MeV. The POD basis accurately reproduces this sharp outline as well as the resonance spikes in the epithermal region. The errors in the cross sections and integral parameters are presented in Tables 7 and 8. In case *a*, all errors are negligible, except for the thermal absorption of ^{135}Xe . In case *b*, the target accuracy is achieved for all the macroscopic cross sections other than fast-to-thermal scattering, for which the error bound is slightly exceeded. Similarly, the isotopic cross sections of H_2O and ^{10}B and the fast-fission cross section of ^{238}U have errors between 0.1% and 0.2%. In case *c*, the deviations in the thermal-group macroscopic cross sections are still negligible, whereas higher errors (between -0.35% and -0.51%) are observed in the fast group. These residual errors are caused by minor imperfections in the prediction of the epithermal spectrum perturbation (Fig. 13(b)). For instance, at 6.67 eV (which corresponds to one of the main resonances of ^{238}U) the reference spectrum change is -17.3%, whereas the computed value is -18.0%. Since the magnitude of the deformation is very high, small discrepancies in the resonance region can result in non-negligible errors in the collapsed cross sections. We have verified that the fast-group errors drop to zero if the cross-section corrections are computed with the reference $\delta\Phi_{\infty,1}(u)$. Another feature of the low-density calculation is the increase in the number of iterations for the convergence of the reconstruction algorithm.

The contributions of the various effects to the cross-section variations are reported in Table 9 for case *c*. The perturbations computed with the rehomogenization-based method are

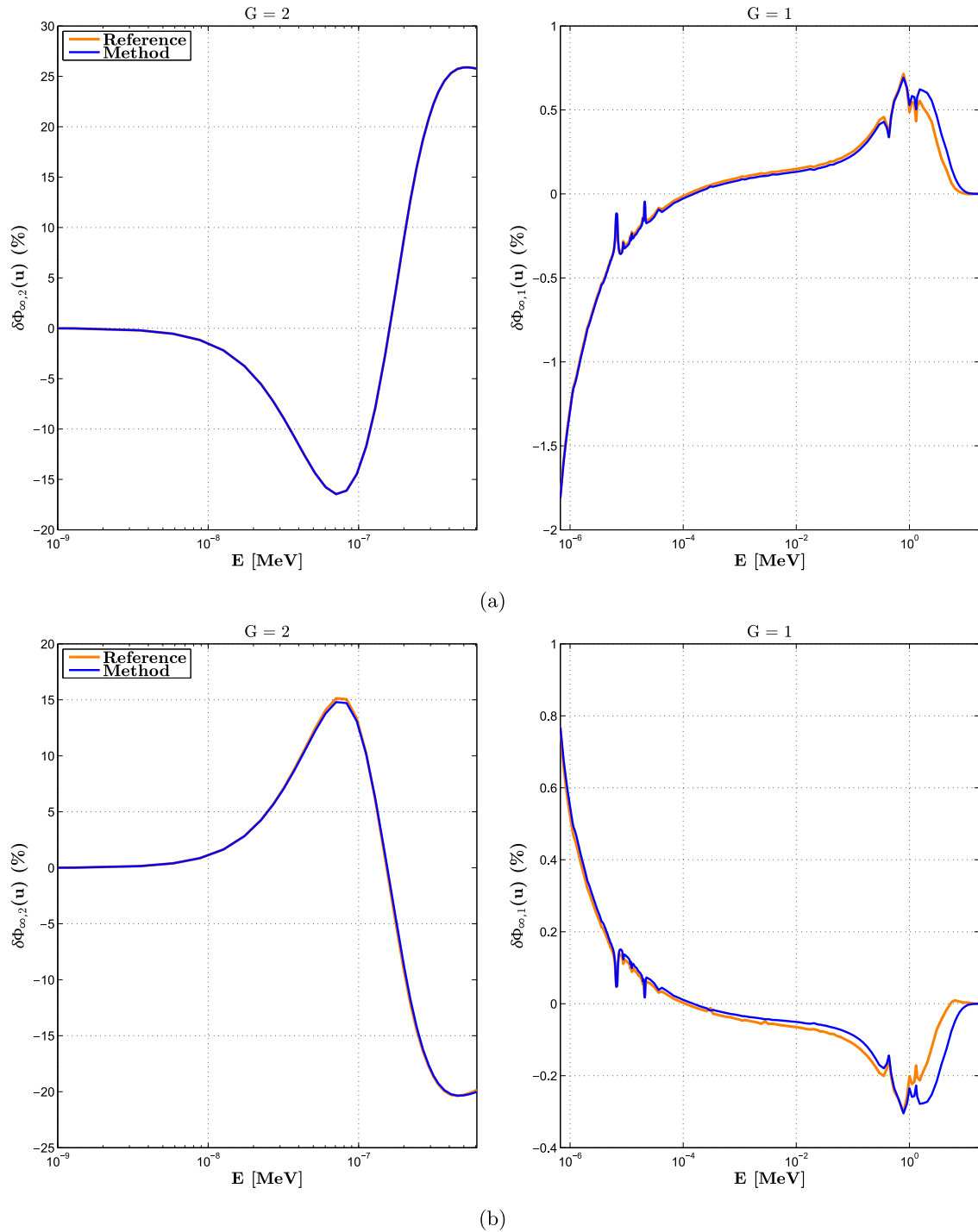


Fig. 10. Spectrum variations (per unit u) versus energy due to the following transitions: (a) from $C_{B_{10}} = 700$ ppm to $C_{B_{10}} = 2450$ ppm (both conditions have $N_{Xe_{135}} = 0$ a/ \AA^3); (b) from $C_{B_{10}} = 700$ ppm and $N_{Xe_{135}} = 4.0 \cdot 10^{-9}$ a/ \AA^3 to $C_{B_{10}} = 0$ ppm and $N_{Xe_{135}} = 0$ a/ \AA^3 .

Table 4

Variations in the boron concentration: errors in the reconstructed macroscopic cross sections and in the main integral parameters, and number of iterations.

Case	$\Delta\Sigma_{a,1}^{\infty}$ (%)	$\Delta\Sigma_{a,2}^{\infty}$ (%)	$\Delta\nu\Sigma_{f,1}^{\infty}$ (%)	$\Delta\nu\Sigma_{f,2}^{\infty}$ (%)	$\Delta\Sigma_{s,1\rightarrow 2}^{\infty}$ (%)	Δk_{∞} [pcm]	$\Delta\Phi_{\infty,G}$ (%)	$\Delta\bar{P}_{\text{fiss}}^{\infty}$ (%)	n_{iter}
a	-0.007	-0.018	0.012	-0.039	-0.02	-13	0.0, -0.004	-0.033	8
b	0.016	0.03	-0.013	0.039	0.031	4	0.0, 0.001	0.033	7

compared to the reference ones. In this example, the spectral and microscopic effects give a relevant contribution to the global variation.

We remark that in this analysis the slowing-down cross section $\Sigma_{s,1\rightarrow 2}^{\infty}$ is not corrected for up-scatter effects. The thermal-to-fast scattering cross section $\Sigma_{s,2\rightarrow 1}^{\infty}$ (which is not addressed in the

Table 5

Variations in the boron concentration: errors (in %) in the reconstructed microscopic cross sections of some relevant isotopes.

Case	H ₂ O		¹⁰ B		¹³⁵ Xe		²³⁵ U				²³⁸ U		
	$\Delta\sigma_{a,2}^\infty$	$\Delta\sigma_{s,1-2}^\infty$	$\Delta\sigma_{a,2}^\infty$	$\Delta\sigma_{a,2}^\infty$	$\Delta\sigma_{a,2}^\infty$	$\Delta\sigma_{a,2}^\infty$	$\Delta\sigma_{a,1}^\infty$	$\Delta\sigma_{a,2}^\infty$	$\Delta\nu\sigma_{f,1}^\infty$	$\Delta\nu\sigma_{f,2}^\infty$	$\Delta\sigma_{a,1}^\infty$	$\Delta\sigma_{a,2}^\infty$	$\Delta\nu\sigma_{f,1}^\infty$
a	0.017	-0.016	0.017	-0.046	-0.021	-0.039	-0.021	-0.039	0.020	0.039	-0.004	-0.038	0.052
b	-0.035	0.030	-0.026	0.016	0.020	0.040	0.020	0.039	0.020	0.039	0.017	0.037	-0.054

Table 6

Variations in the macroscopic cross sections and integral parameters due to the transition from 700 ppm to 2450 ppm (case a). Since neither the water density nor the xenon level changes and the microscopic effect of boron concentration is neglected, only the direct and spectral effects are present. The reference values of the perturbed cross sections are: $\Sigma_{a,1}^\infty = 0.008891 \text{ cm}^{-1}$, $\Sigma_{a,2}^\infty = 0.076932 \text{ cm}^{-1}$, $\nu\Sigma_{f,1}^\infty = 0.004830 \text{ cm}^{-1}$, $\nu\Sigma_{f,2}^\infty = 0.080188 \text{ cm}^{-1}$, and $\Sigma_{s,1-2}^\infty = 0.017106 \text{ cm}^{-1}$.

	$\delta\Sigma_{a,1}^\infty$ (%)	$\delta\Sigma_{a,2}^\infty$ (%)	$\delta\nu\Sigma_{f,1}^\infty$ (%)	$\delta\nu\Sigma_{f,2}^\infty$ (%)	$\delta\Sigma_{s,1-2}^\infty$ (%)	δk_∞ [pcm]	$\delta\bar{\Phi}_{\infty,G}$ (%)	$\delta\bar{P}_{fiss}^\infty$ (%)
Direct	4.80	28.11	0.0	0.0	0.0	-20950	4.92, -17.76	-13.99
Spectr. (Ref.)	-0.336	-3.50	-0.284	-2.78	-1.92	-250	-0.085, 0.306	-1.73
Global (Ref.)	4.46	24.61	-0.284	-2.78	-1.92	-21200	4.83, -17.45	-15.72

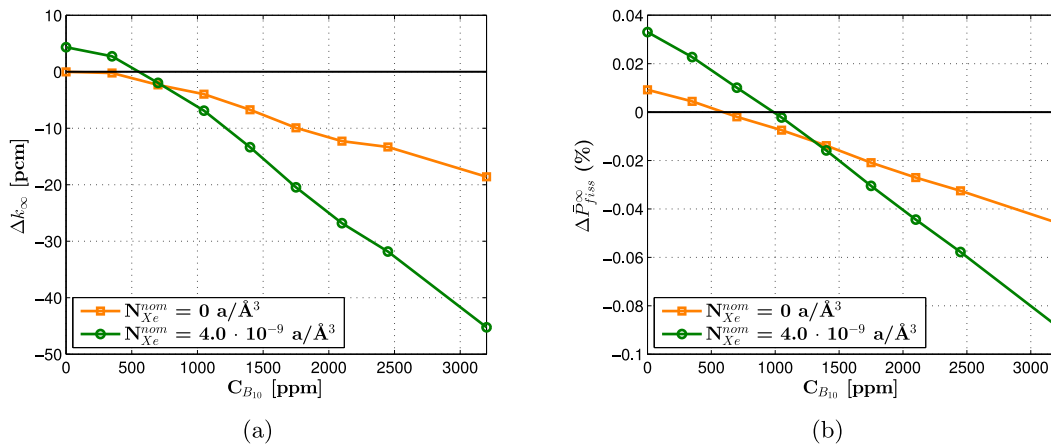


Fig. 11. Errors in the (a) multiplication factor and (b) total fission power versus the boron concentration. The case with $N_{Xe135}^{nom} = 0 \text{ a}/\text{\AA}^3$ corresponds to a variation in $C_{B_{10}}$ only.

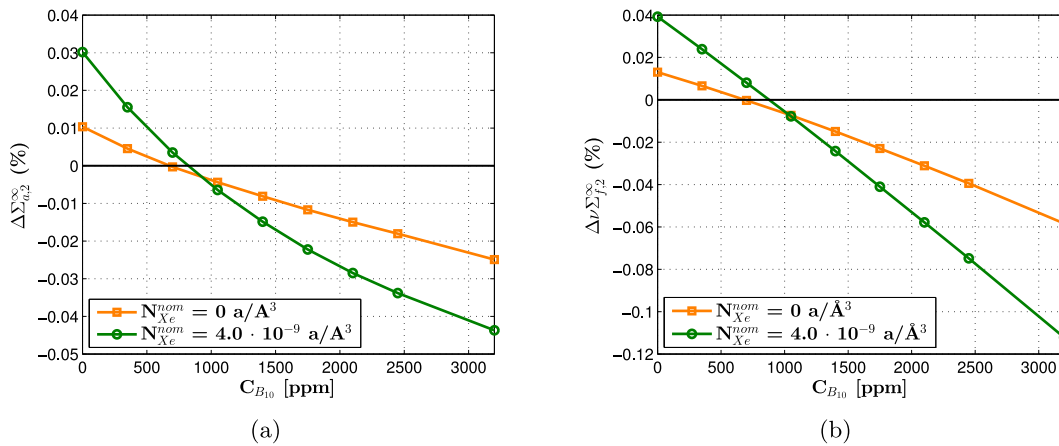


Fig. 12. Errors in the thermal-group (a) absorption and (b) production cross sections versus the boron concentration.

previous tables) has been considered explicitly and also rehomogenized. For example, the errors $\Delta\Sigma_{s,2-1}^\infty$ of cases b and c are -0.087% and -0.052%, respectively. The components of the reference variation $\delta\Sigma_{s,2-1}^{\infty,ref}$ from the nominal state are:

- 21.1% (direct effect), -26.5% (spectral and microscopic effects), and -5.4% (global effect) in case b;
- -48.7% (direct effect), 63.9% (spectral and microscopic effects), and -15.2% (global effect) in case c.

A parametric analysis similar to that of Section 3.1.2 has been made for the water density. The errors versus ρ_{H_2O} are shown in Figs. 14–17 for various quantities. At densities between 0.51 and 0.81 g/cm³, the absolute values of the cross-section errors are below 0.1% in the fast group and 0.03% in the thermal one, and the absolute values of the deviations in k_∞ are below 20 pcm. At 0.21 g/cm³, the highest error is found in fast-to-thermal scattering (-0.63% when the xenon concentration also varies).

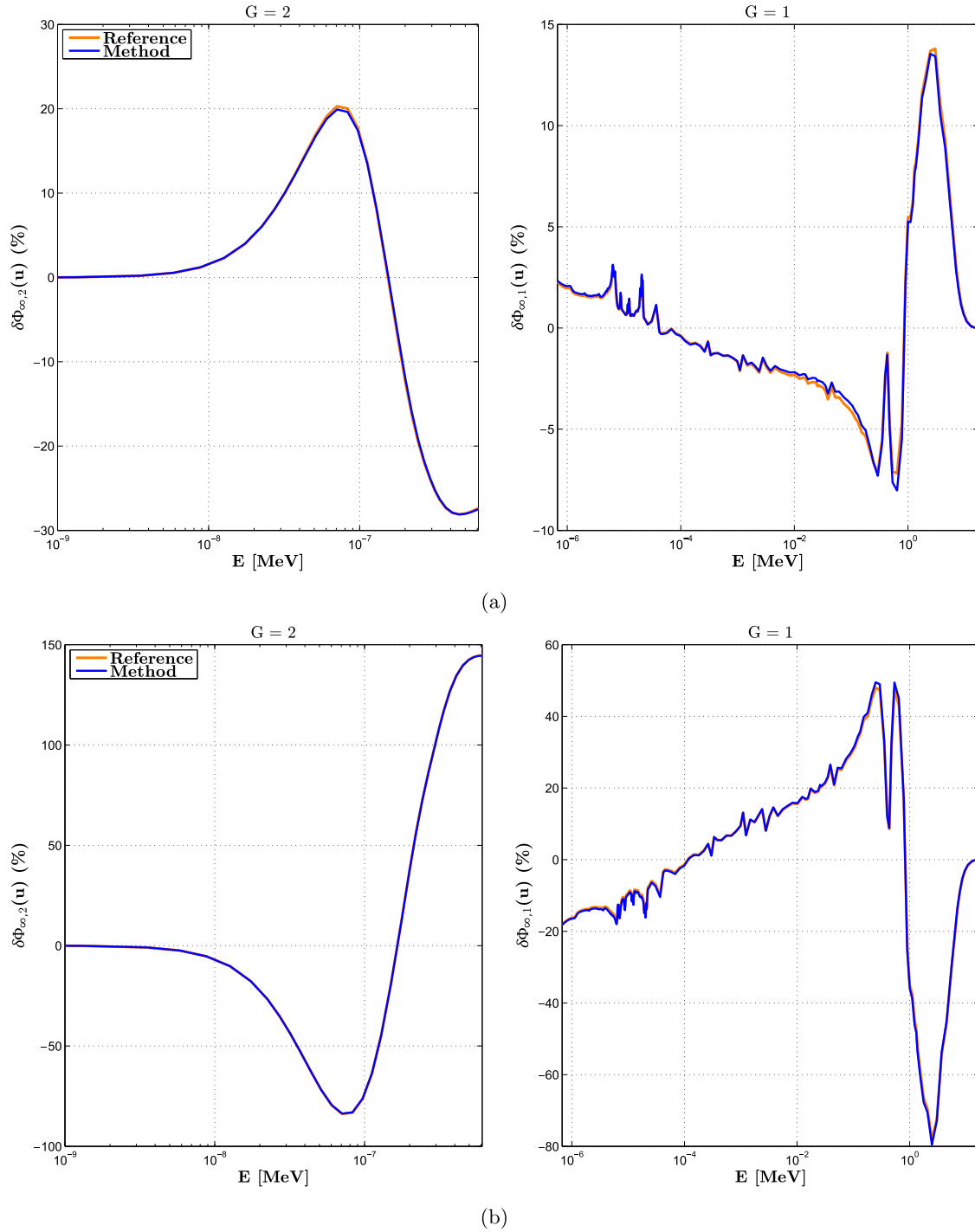


Fig. 13. Spectrum variations (per unit u) versus energy due to the following transitions: (a) from $\rho_{H_2O} = 0.7 \text{ g/cm}^3$ and $N_{Xe135} = 4.0 \cdot 10^{-9} \text{ a/\AA}^3$ to $\rho_{H_2O} = 0.91 \text{ g/cm}^3$ and $N_{Xe135} = 0 \text{ a/\AA}^3$; (b) from $\rho_{H_2O} = 0.7 \text{ g/cm}^3$ to $\rho_{H_2O} = 0.21 \text{ g/cm}^3$ (both conditions have $N_{Xe135} = 0 \text{ a/\AA}^3$).

Table 7

Variations in the water density: errors in the reconstructed macroscopic cross sections and in the main integral parameters, and number of iterations.

Case	$\Delta\Sigma_{a,1}^{\infty}$ (%)	$\Delta\Sigma_{a,2}^{\infty}$ (%)	$\Delta\nu\Sigma_{f,1}^{\infty}$ (%)	$\Delta\nu\Sigma_{f,2}^{\infty}$ (%)	$\Delta\Sigma_{s,-2}^{\infty}$ (%)	Δk_{∞} [pcm]	$\Delta\bar{\Phi}_{\infty,G}$ (%)	$\Delta\bar{P}_{fiss}^{\infty}$ (%)	n_{iter}
a	0.067	-0.002	-0.018	0.013	0.034	-9	-0.008, 0.027	0.031	7
b	0.065	-0.019	-0.05	0.025	0.115	26	-0.035, 0.1	0.098	6
c	-0.361	0.062	-0.374	0.046	-0.506	-35	0.044, -0.522	-0.434	17

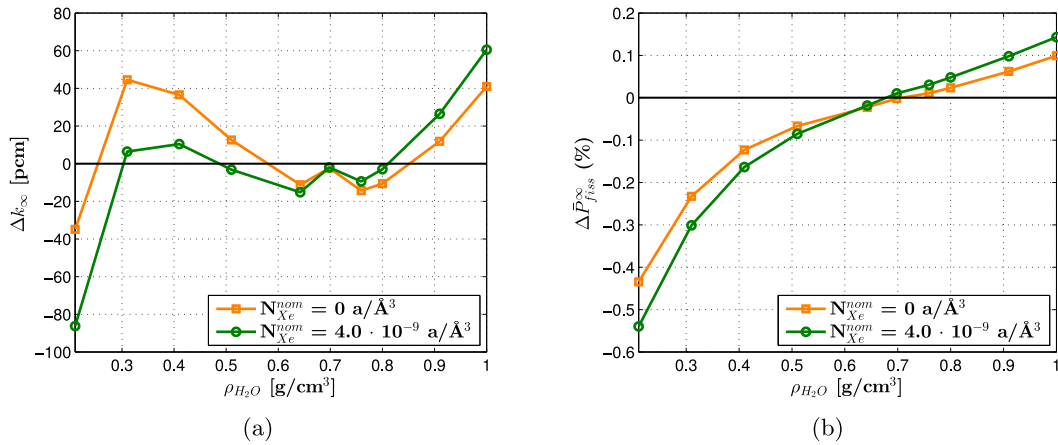
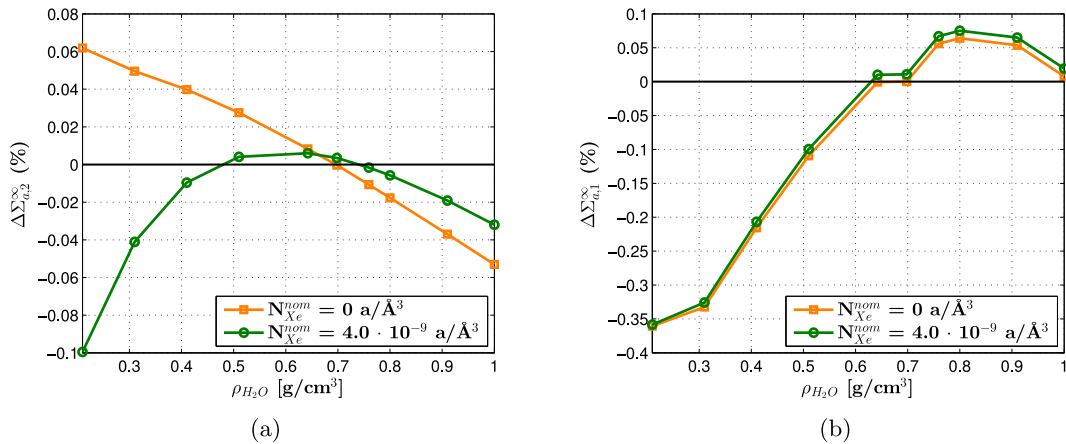
Table 8

Variations in the water density: errors (in %) in the reconstructed microscopic cross sections of some relevant isotopes.

Case	H ₂ O		¹⁰ B	¹³⁵ Xe	²³⁵ U				²³⁸ U		
	$\Delta\sigma_{a,2}^{\infty}$	$\Delta\sigma_{s,1-2}^{\infty}$	$\Delta\sigma_{a,2}^{\infty}$	$\Delta\sigma_{a,2}^{\infty}$	$\Delta\sigma_{a,1}^{\infty}$	$\Delta\sigma_{a,2}^{\infty}$	$\Delta\nu\sigma_{f,1}^{\infty}$	$\Delta\nu\sigma_{f,2}^{\infty}$	$\Delta\sigma_{a,1}^{\infty}$	$\Delta\sigma_{a,2}^{\infty}$	$\Delta\nu\sigma_{f,1}^{\infty}$
a	-0.053	0.034	-0.053	-0.263	0.019	0.014	0.018	0.013	0.087	0.012	-0.063
b	-0.148	0.115	-0.148	-0.098	0.071	0.025	0.065	0.025	0.072	0.021	-0.189
c	0.297	-0.538	0.297	-0.748	-0.64	0.046	-0.568	0.046	-0.306	0.041	-0.071

Table 9Variations in the macroscopic cross sections and integral parameters due to the transition from 0.7 g/cm³ to 0.21 g/cm³ (case c). The reference values of the perturbed cross sections are: $\Sigma_{a,1}^{\infty} = 0.006768$ cm⁻¹, $\Sigma_{a,2}^{\infty} = 0.046244$ cm⁻¹, $\nu\Sigma_{f,1}^{\infty} = 0.003907$ cm⁻¹, $\nu\Sigma_{f,2}^{\infty} = 0.071230$ cm⁻¹, and $\Sigma_{s,1-2}^{\infty} = 0.004003$ cm⁻¹.

	$\delta\Sigma_{a,1}^{\infty}$ (%)	$\delta\Sigma_{a,2}^{\infty}$ (%)	$\delta\nu\Sigma_{f,1}^{\infty}$ (%)	$\delta\nu\Sigma_{f,2}^{\infty}$ (%)	$\delta\Sigma_{s,1-2}^{\infty}$ (%)	δk_{∞} [pcm]	$\delta\Phi_{\infty,G}$ (%)	$\delta\bar{P}_{fiss}^{\infty}$ (%)
Direct	-2.68	-13.72	0.0	0.0	-68.69	-11520	15.96, -57.60	-45.38
Spectr. + micr. (Ref.)	-17.81	-11.38	-19.35	-13.64	-8.35	-3711	1.85, -6.68	-12.96
Spectr. + micr. (calc.)	-18.09	-11.33	-19.65	-13.60	-8.47	-3745	1.90, -6.86	-13.14
Global (Ref.)	-20.48	-25.1	-19.35	-13.64	-77.05	-15230	17.81, -64.27	-58.34

**Fig. 14.** Errors in the (a) multiplication factor and (b) total fission power versus the moderator density. The case with $N_{Xe135}^{nom} = 0$ a/Å³ corresponds to a variation in ρ_{H_2O} only.**Fig. 15.** Errors in the (a) thermal- and (b) fast-group absorption cross sections versus the moderator density.

3.1.4. Combined variations in the three parameters

We now assess the performance of the method for simultaneous variations in the three parameters. In the following, we will only consider nominal conditions with $N_{Xe135} = 4.0 \cdot 10^{-9}$ a/Å³. The perturbation δN_{Xe135} is therefore fixed at $-4.0 \cdot 10^{-9}$ a/Å³.

Table 10 reports the numerical errors for various perturbed states. A more general overview is given in Figs. 18–20, which

show the deviations in k_{∞} , $\Sigma_{a,2}^{\infty}$ and $\nu\Sigma_{f,2}^{\infty}$ along the whole range of variation of ρ_{H_2O} and $C_{B_{10}}$. At water densities between 0.51 and 0.81 g/cm³, the absolute values of the errors in k_{∞} are (i) lower than 25 pcm if $C_{B_{10}}$ varies in the range [0 ppm, 1500 ppm], and (ii) lower than 40 pcm if $C_{B_{10}}$ varies in the range [1500 ppm, 2000 ppm]. The errors in $\Sigma_{a,2}^{\infty}$ are well below 0.1% in most of the state-parameter domain, whereas the deviations in $\nu\Sigma_{f,2}^{\infty}$ remain

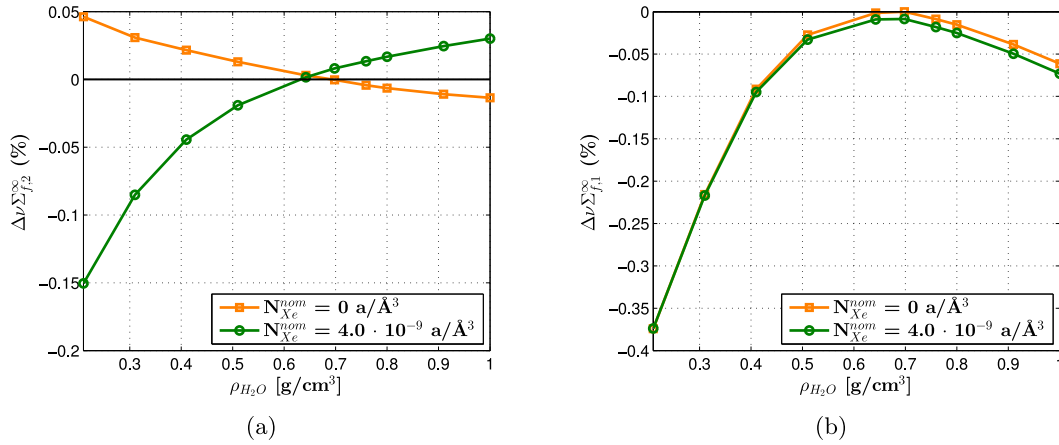


Fig. 16. Errors in the (a) thermal- and (b) fast-group production cross sections versus the moderator density.

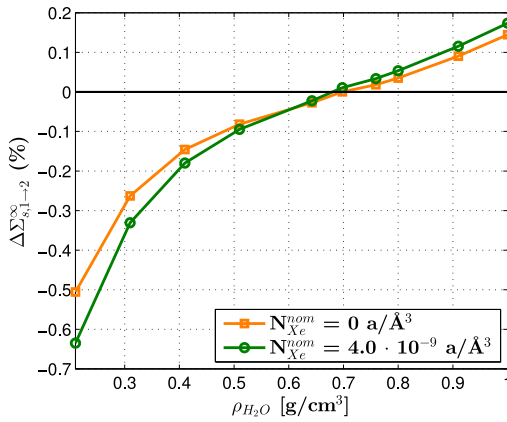


Fig. 17. Error in the fast-to-thermal scattering cross section versus the moderator density.

below this bound if $C_{B_{10}} < 2000$ ppm and $\rho_{H_2O} > 0.41$ g/cm³. The errors in the aforementioned quantities become negative for boron concentrations above a certain value. At $\rho_{H_2O} = 0.21$ g/cm³, the dependence on the boron concentration is negligible (especially in k_∞ and $\Sigma_{a,2}^\infty$). Similarly, deviations in the fast group only depend on the moderator density and almost do not vary with the boron concentration. This can be observed in Fig. 21, which shows the behavior of the error in $\Sigma_{a,1}^\infty$.

3.2. Application to a heterogeneous multiassembly configuration

We now apply the method to predict the combined effects of perturbations in the state parameters and interassembly neutron

leakage on the node-averaged flux spectrum. The analysis is made on a colorset configuration (namely, a four-assembly set with reflective boundary conditions along the assembly centerlines). The fuel assemblies in the colorset are of the same type as that simulated in Section 3.1 (1.8%-enriched UO₂). Two clusters of twenty-four black control rods each are inserted into two of the four bundles. The type of the control elements is AIC (silver-indium-cadmium), with the following mass percent composition: 80% ⁴⁷Ag, 15% ⁴⁸Cd, and 5% ⁴⁹In. The assembly arrangement in the colorset and the internal layout of the rodded bundle are shown in Fig. 22. The colorset is simulated at zero burn-up and at normal operating conditions ($T_{fuel} = 851.5$ K, $T_{H_2O} = 586.1$ K, $\rho_{H_2O} = 0.71$ g/cm³), without thermal-hydraulic feedback or fuel depletion. There is no boron diluted in the moderator ($C_{B_{10}} = 0$ ppm). Hence, the deviations of the local conditions from the nominal ones are $\delta C_{B_{10}} = -700$ ppm and $\delta N_{Xe_{135}} = -4.0 \cdot 10^{-9}$ a/Å³. The change in the water density is negligible. The reference effective multiplication factor and control-rod bank worth from APOLLO2-A are $k_{eff} = 0.98847$ and $w_{CR} = 21840$ pcm, respectively. The reference assembly-averaged fission power \bar{P}_{fiss} is 1.216 in the unrodded assembly and 0.784 in the rodded one.

The nodal simulations of the colorset are performed with the ARTEMIS code (Hobson et al., 2013), in which a beta-testing version of the rehomogenization-based cross-section model has been implemented. Also in this case, the parameterized libraries are generated with APOLLO2-A. We present the results of the following calculations:

- with infinite-medium cross sections computed without the critical-buckling correction (a);
- with standard infinite-medium cross sections and the critical-buckling correction (b);

Table 10

Three-parameter variations: errors in the reconstructed macroscopic cross sections and in the main integral parameters, and number of iterations. The perturbed xenon concentration is 0 a/Å³ in all test cases.

ρ_{H_2O} [g/cm ³]	$C_{B_{10}}$ [ppm]	$\Delta\Sigma_{a,1}^\infty$ (%)	$\Delta\Sigma_{a,2}^\infty$ (%)	$\Delta\nu\Sigma_{f,1}^\infty$ (%)	$\Delta\nu\Sigma_{f,2}^\infty$ (%)	$\Delta\Sigma_{s,1\rightarrow 2}^\infty$ (%)	Δk_∞ [pcm]	$\Delta\Phi_{\infty,G}$ (%)	$\Delta\bar{P}_{fiss}^\infty$ (%)	n_{iter}
0.41	0	-0.198	-0.001	-0.102	-0.015	-0.154	26	0.024, -0.129	-0.132	9
0.51	1200	-0.104	-0.004	-0.028	-0.041	-0.111	-13	-0.018, -0.09	-0.107	9
0.64	800	0.009	0.004	-0.008	-0.003	-0.026	-15	0.006, -0.022	-0.021	7
0.76	1600	0.061	-0.028	-0.012	-0.030	0.012	-23	-0.008, 0.031	-0.002	7
0.81	200	0.079	0.018	-0.027	0.04	0.066	0	-0.012, 0.037	0.062	7
0.81	1400	0.071	-0.029	-0.021	-0.017	0.038	-13	-0.015, 0.053	0.024	6
0.91	2000	0.063	-0.065	-0.044	-0.044	0.095	-1	-0.034, 0.125	0.056	6
1.0	2600	0.026	-0.098	-0.067	-0.075	0.154	7	-0.053, 0.198	0.084	7

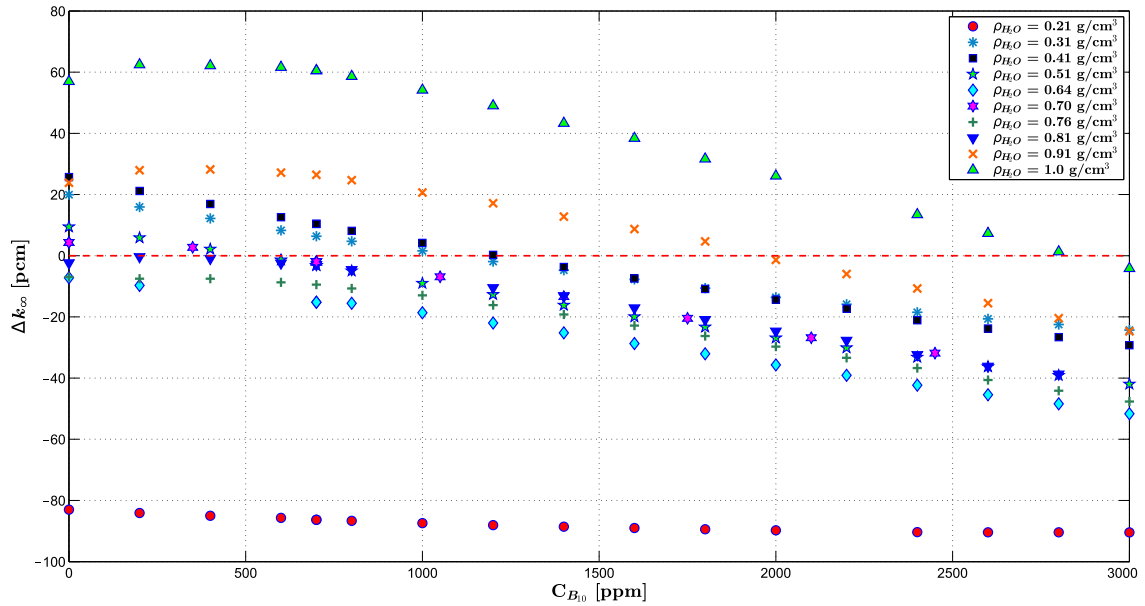


Fig. 18. Error in the infinite-medium multiplication factor as a function of the boron concentration (on the x-axis) and of the moderator density (markers). In all simulated states, the variation in the xenon density is $\delta N_{Xe135} = -4.0 \cdot 10^{-9} \text{ a}/\text{\AA}^3$.

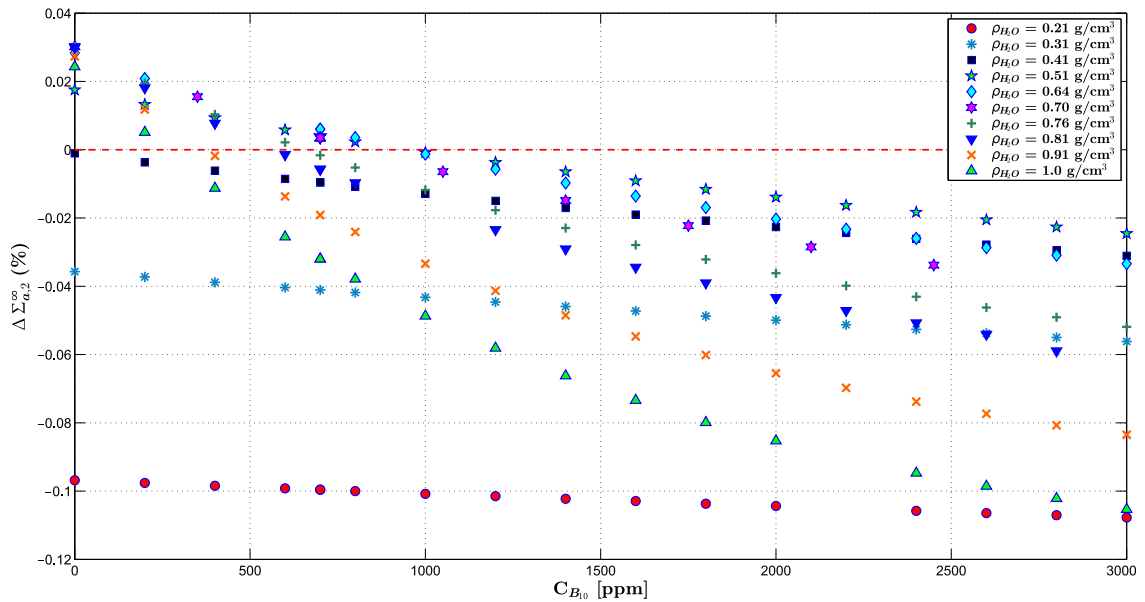


Fig. 19. Error in the thermal-group absorption cross section as a function of the boron concentration (on the x-axis) and of the moderator density (markers).

- with cross sections corrected by the reference spectral defect (c);
- with spectral rehomogenization of the infinite-medium cross sections interpolated at p_{loc} (d);
- with spectral rehomogenization of the infinite-medium cross sections interpolated at p_{nom} (e).

Calculation *b* is currently the most widely used approach in nodal codes. In calculation *c*, the reference spectral corrections are obtained by collapsing the 281-group macroscopic cross sections in the infinite lattice at the local conditions with the reference environmental spectrum variation from APOLLO2-A. This type of correction does not take into account the spatial effects of the environment (i.e., the spatial homogenization error) and is therefore only partial. However, since it fully corrects the node-

averaged spectral error, we take it as the reference for our method. In calculation *d*, only the spectral effects of the environment are modeled by rehomogenization, as described in our previous work (Gamarino et al., 2018a,b). Calculation *e* is the one that fully applies the method proposed in this paper. In both simulations *d* and *e*, rehomogenization is applied with the diffusive leakage model and the semi-analytic basis investigated in Gamarino et al. (2018a). This basis consists of Chebyshev polynomials of the first kind in both coarse energy groups, combined with the neutron emission spectrum from fission in the fast group.

In ARTEMIS, the two-group diffusion coefficient is computed from the buckling coefficient (set to the critical value by default) and the leakage cross section $\Sigma_{leak,G}^{\infty} = D_G^{\infty} B^2$. The same applies to the fine-group diffusion coefficient for the calculation of the rehomogenization parameters $h_{R,D,G,j}$ and $h_{V,D,G,i,j}$ (Eq. (40)). In order to

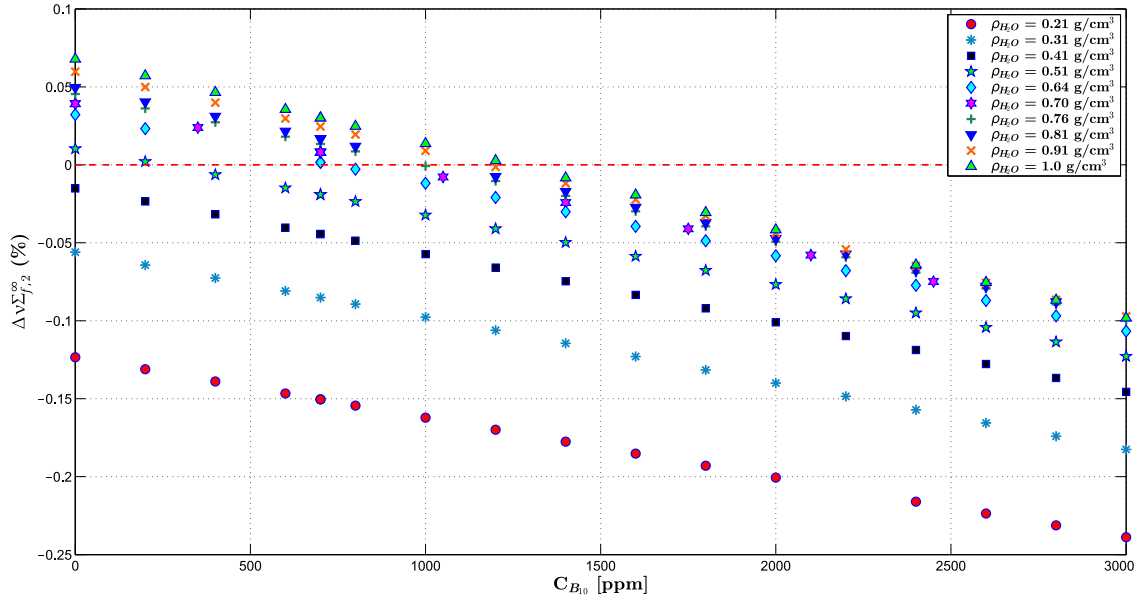


Fig. 20. Error in the thermal-group production cross section as a function of the boron concentration (on the x-axis) and of the moderator density (markers).

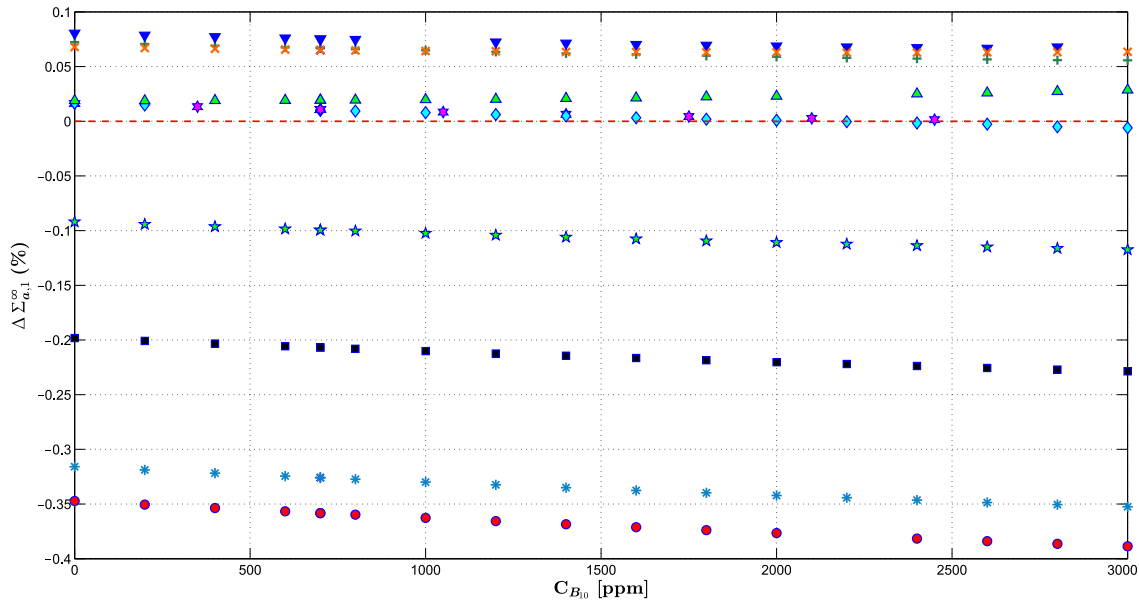


Fig. 21. Error in the fast-group absorption cross section as a function of the boron concentration (on the x-axis) and of the moderator density (markers). The legend is the same as in Figs. 18–20.

be consistent with the methodology of Section 2.1.1, which has been derived for the zero-buckling case, the nodal data for simulations other than b are generated with the smallest user-defined value of B^2 accepted by APOLLO2-A ($B^2 = 10^{-7} \text{ cm}^{-2}$). This value is four orders of magnitude lower than the critical one in both fuel bundles ($B_{\text{crit}}^2 = 3.24 \cdot 10^{-3} \text{ cm}^{-2}$ in the unrodded assembly, and $B_{\text{crit}}^2 = -4.37 \cdot 10^{-3} \text{ cm}^{-2}$ in the rodded assembly). Compared to the zero-buckling case, the differences in all the computed cross sections are below 0.005%. Hence, with this choice no inconsistency is introduced in the application of the methodology.

Fig. 23 shows (i) the change in the infinite-medium spectrum due to the aforementioned perturbations in the state parameters [$\delta\Phi_{\infty,G}(u) = \Phi_{\infty,G}^{\text{loc}}(u) - \Phi_{\infty,G}^{\text{nom}}(u)$], and (ii) the deformation of the spectrum in the colorset environment at the local conditions

[$\delta\Phi_{\text{env},G}(u) = \Phi_{\text{env},G}^{\text{loc}}(u) - \Phi_{\infty,G}^{\text{loc}}(u)$]. The variations in both $C_{B_{10}}$ and $N_{X_{e135}}$ from their nominal values contribute to a reduction in absorption, thus thermalizing the spectrum in the two assemblies. Neutron streaming hardens the spectrum in the unrodded assembly and thermalizes it in the rodded one. The neighbor-effect component is preeminent in the fast group, whereas the state-parameter change has the highest impact in the thermal group.

Fig. 24 depicts the overall spectrum variation [$\delta\Phi_G(u) = \Phi_{\text{env},G}^{\text{loc}}(u) - \Phi_{\infty,G}^{\text{nom}}(u)$] estimated with calculation e . The computed curves accurately predict the global behavior of the reference. Minor deviations from the transport solution are mainly found in the thermal group and in the high-energy region of the fast group (at $E > 0.1 \text{ MeV}$). These deviations are due partly to the limited fitting capability of the polynomial basis functions

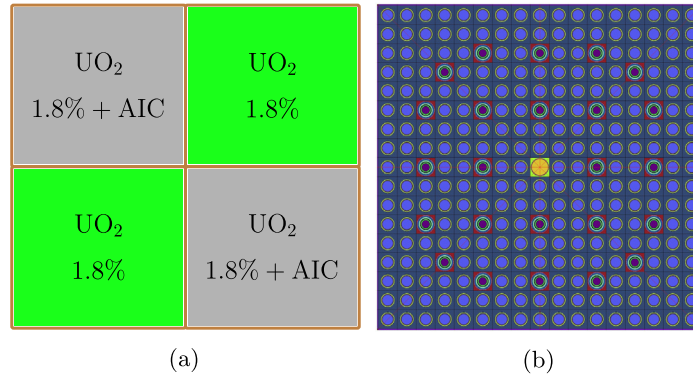


Fig. 22. (a) Colorset arrangement and (b) internal layout of the fuel assembly with twenty-four AIC control rods. The ^{235}U enrichment in the colorset is uniform (1.8% in all fuel pins). An empty guide tube for the instrumentation is present at the center of the rodded assembly.

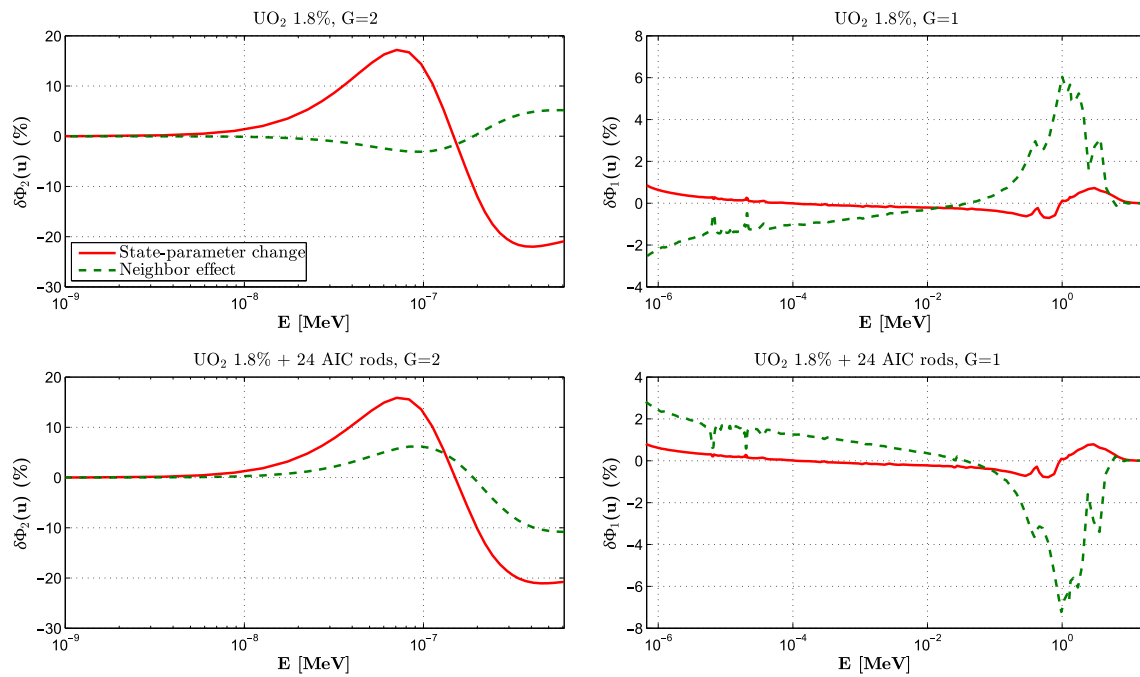


Fig. 23. Components of the spectrum variation (per unit u) in the unrodded and rodded assemblies of the colorset example: (i) perturbation in the infinite medium due to the transition from the nominal to the local conditions (solid lines), and (ii) perturbation in the environment due to neighbor effects (dashed lines).

and partly to inherent flaws of the diffusive approximation of the leakage spectrum, whose outcome is shown in Fig. 25. The leakage function computed with this approach is very precise in the epithermal region and in the low-energy region of the thermal group ($E < 0.25$ eV), whereas it suffers from some inaccuracy in the range [0.25 eV, 0.625 eV] and in the fission-emission region. For the above set of calculations, Table 11 reports the errors in the nodal cross sections of the two assemblies. The critical-buckling approach significantly overcorrects the fast-group cross sections. The corrections computed with calculation e go in the right direction and are close to the reference ones (calculation c), except for thermal absorption in the rodded assembly (for which yet the error decreases compared to the infinite-medium values). The improvement over calculations a and b is apparent. Table 12 shows the errors in the main integral parameters and the number of power iterations for the convergence of the eigenvalue calculation. The power-error value out of parentheses refers to the total power, whereas the two values within parentheses correspond to the fast- and thermal-group power, respectively. Calculation e produces better estimates of the integral parameters than those ensu-

ing from standard interpolation of the infinite-medium cross sections. The method strongly reduces the overestimation of the control-rod bank worth observed with the conventional B_{crit}^2 approach (the small error found with calculation a is instead the result of favorable error cancellation). Similar considerations hold for the environmental rehomogenization (calculation d). We remark that the residual errors of our reference calculation are ascribable to the spatial component of the homogenization defects (Dall'Osso, 2014; Gamarino et al., 2016), which cannot be corrected by spectral rehomogenization. These errors are higher in k_{eff} and in the thermal fission power.

4. Discussion

4.1. Numerical features and impact on the cross-section model

For a standard PWR UO_2 assembly (as the one analyzed in this work), cross-section libraries commonly consist of about 3000 calculation points. With the rehomogenization-based model, the

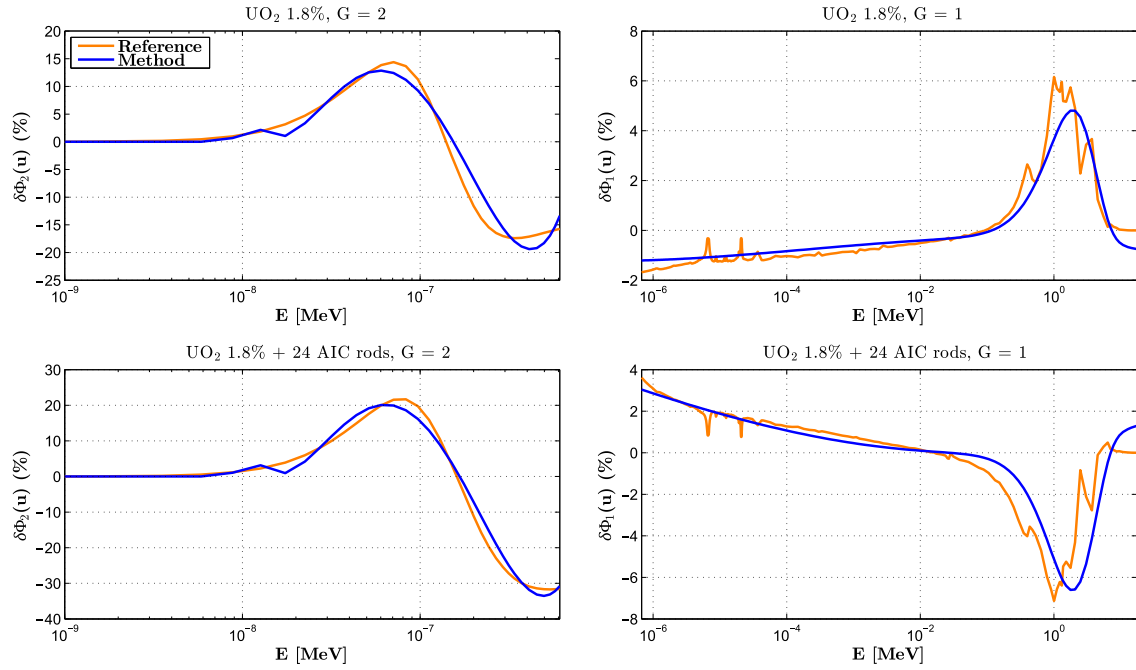


Fig. 24. Spectrum variation (per unit u) between the colorset environment in the local conditions and the infinite lattice in the nominal conditions, as computed by the rehomogenization-based reconstruction algorithm with the diffusive leakage model (calc. e).

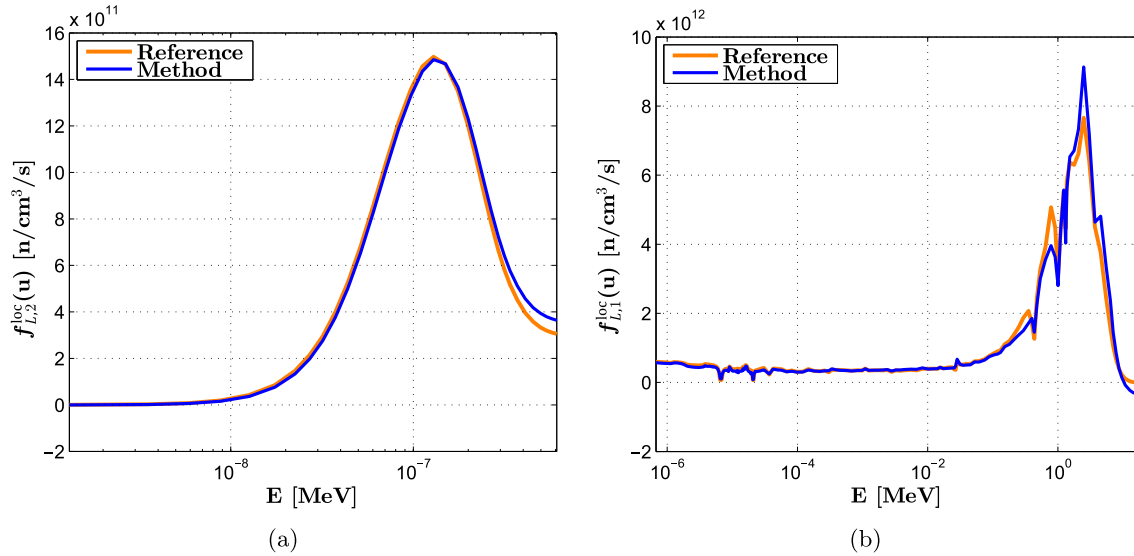


Fig. 25. (a) Thermal- and (b) fast-group leakage spectra in the unrodded assembly, as computed with the diffusive approximation applied to calculation e . The curves are normalized to the reference coarse-group assembly-averaged leakage. Units are in neutrons/(cubic centimeters · second).

Table 11
Errors in the nodal cross sections of the colorset benchmark problem.

	UO ₂ 1.8%					UO ₂ 1.8% + 24 AIC rods				
	$\Sigma_{a,1}$	$\Sigma_{a,2}$	$\nu\Sigma_{f,1}$	$\nu\Sigma_{f,2}$	$\Sigma_{s,1-2}$	$\Sigma_{a,1}$	$\Sigma_{a,2}$	$\nu\Sigma_{f,1}$	$\nu\Sigma_{f,2}$	$\Sigma_{s,1-2}$
Reference [cm^{-1}]	0.00825	0.0554	0.00483	0.0833	0.0172	0.0115	0.0810	0.00472	0.0849	0.0151
Simulation	Errors (%)									
Inf. med., no B_{crit}^2 (a)	1.39	0.55	0.36	0.60	3.40	-1.63	0.78	-0.45	-0.89	-4.42
Inf. med., B_{crit}^2 (b)	-0.82	0.41	-0.35	0.45	-1.08	1.95	0.91	0.66	-0.70	1.54
Ref. $\delta\Sigma_C^{\text{spec}}$ (c)	-0.05	0.19	-0.33	0.22	-0.28	0.47	1.37	0.43	-0.06	0.11
Rehom. at p_{loc} (d)	-0.26	0.23	-0.26	0.26	-0.23	0.54	1.20	0.31	-0.31	1.0
Rehom. at p_{nom} (e)	-0.25	0.02	-0.35	0.06	0.31	0.44	0.65	0.24	-0.38	0.04

Table 12

Number of power iterations (n_{iter}) and errors in the effective multiplication factor, control-rod bank worth, assembly-averaged flux, and assembly-averaged fission power of the colorset benchmark problem.

Simulation	n_{iter}	Δk_{eff} [pcm]	Δw_{CR} (%)	UO ₂ 1.8%		UO ₂ 1.8% + 24 AIC rods	
				$\Delta \bar{\Phi}_G$ (%)	$\Delta \bar{P}_{\text{fiss}}$ (%)	$\Delta \bar{\Phi}_G$ (%)	$\Delta \bar{P}_{\text{fiss}}$ (%)
Inf. med., no B_{crit}^2 (a)	6	80	0.37	-0.47, 1.65	2.51 (0.52, 2.89)	0.62, -3.14	-3.91 (-0.61, -4.78)
Inf. med., B_{crit}^2 (b)	6	-687	-3.15	0.14, -0.51	0.41 (-0.25, 0.55)	0.083, -0.42	-0.64 (0.30, -0.92)
Ref. $\delta \Sigma_G^{\text{spec}}$ (c)	6	-425	-1.95	0.03, -0.12	0.70 (-0.07, 0.86)	0.26, -1.29	-1.10 (0.09, -1.43)
Rehom. at p_{loc} (d)	10	-387	-1.87	-0.01, 0.05	0.98 (0.04, 1.17)	0.30, -1.54	-1.53 (-0.05, -1.94)
Rehom. at p_{nom} (e)	13	-196	-0.9	-0.12, 0.42	0.77 (0.0, 0.91)	0.14, -0.73	-1.20 (0.0, -1.51)

boron-concentration axis can be removed. Along the water-density and xenon-concentration axes, only few points must be kept, without cross calculations, to account for the effects of variations in the fine-group microscopic cross sections. The number of lattice simulations and table points decreases by a factor of approximately 9 if the water-density self-shielding coefficients are only computed along the burn-up axis, or 7 if they are also computed along the fuel-temperature axis. In an industrial utilization where the methodology is applied to reconstruct the cross sections directly in the real environment, the computational burden of the lattice calculations is also reduced because of the elimination of the critical-spectrum iterations. The memory requirement for the storage of the rehomogenization coefficients is negligible compared to the global memory saving.

The contraction of the interpolation hyperspace also has a beneficial effect on the on-line reconstruction phase. This step usually takes up a significant fraction of the overall run time of the nodal calculation. For example, Table 13 reports the run-time statistics of a 900-MW PWR reactor full-core simulation with standard six-axes interpolation in ARTEMIS. Almost half of the computing time is used by the cross-section module. This high fraction is due to the optimization of the nodal solution strategy in the flux solver (van Geemert, 2014). If the rehomogenization-based reconstruction is applied to compute the single-assembly cross sections (Section 2.1), the number of iterations (each of which consists of the solution of a linear system with rank 8) is generally between 6 and 8. Slower convergence is only found at very low water-density values (Tables 7 and 10). This fraction of the core-calculation run time can be easily minimized via parallelization of the algorithm. If the environmental approach is chosen (Section 2.2), the number of flux iterations increases. For instance, an increase by a factor of 2.17 has been observed in the colorset benchmark problem of Section 3.2 (Table 12). However, this test case has been simulated without thermal feedback to validate the rehomogenization-based strategy against the reference solution from APOLLO2-A. In an actual core calculation, the method would be embedded in the iterations between the flux solver and the thermal-hydraulic calculation (see Fig. 6). The slowdown in the convergence of the eigenvalue calculation would thus be mitigated. Moreover, as observed in Table 13, the contribution of the nodal flux solver to the overall run time of the core calculation is

Table 13

Distribution of a full-core simulation run-time among the main modules for a 900-MW PWR core. The values refer to the ARTEMIS nodal code with traditional six-axes interpolation.

Module	Run time (%)
Cross-section reconstruction	48.9
Flux solver	9.58
Dehomogenization	1.17
Depletion solver	31.7
Thermal-hydraulics	0.26
Others	8.39

about five times smaller than that of the standard interpolation-based reconstruction phase. Therefore, the gain due to the decrease in the number of interpolation axes would prevail over the additional iterations at the flux-solver level.

Isotopic rehomogenization (Eq. (35)) allows modeling the spectral effects of the environment and of the local physical conditions on the microscopic cross sections of relevant nuclides (such as fissile elements, the main fission products and actinides, burnable absorbers, and control elements). Hence, node-averaged history effects due to differences between the off-nominal depletion in the real environment and the single-assembly reference base depletion can be fully accounted for by combining the proposed method with a microscopic depletion model.

Our rehomogenization-based strategy is valid for an arbitrary number of energy groups of the nodal cross sections and can be applied to reactor types other than PWRs. For example, in BWR core analysis one could take advantage of this approach to model the spectral effects of the instantaneous coolant and moderator void fractions (or densities) and, potentially, of the coolant void (or density) history as well. When retaining the boron concentration in the parameterization (see Section 1), the interpolation hyperspace would thus be reduced by four to five axes. Another feature of the method is that it can be used to reconstruct the cross sections in subcritical states, not only in core operation of critical reactors, but also in the presence of a neutron source. This requires to compute the projection coefficients of the neutron-source emission spectrum $S_G(u)$ on the weighting functions $W_{Gj}(u)$:

$$\Psi_{Gj} = \int_0^1 du S_G(u) W_{Gj}(u). \quad (43)$$

This source term is to be added to the right-hand side of Eq. (16). Our strategy can therefore be used for safety analyses of cold shut-down states. Furthermore, it can be easily integrated into the cross-section model of accelerator-driven subcritical reactors.

4.2. On the modal approach

In the tests on single-assembly configurations (Section 3.1), we have used basis and weighting functions built with the POD approach. A similar study has been made with the semi-analytic modes (i.e., Chebyshev polynomials and the fission-emission spectrum) used for the heterogeneous multiassembly benchmark problem in Section 3.2. The results are summarized here for two sample perturbations without xenon variation: a transition to $C_{B_{10}} = 2450$ ppm (case a of Section 3.1.2), and a transition to $\rho_{H_2O} = 0.21$ g/cm³ (case b of Section 3.1.3).

The computed spectrum variations and numerical errors are shown in Fig. 26 and Table 14. A significant loss of accuracy is found in the prediction of the fast-group spectrum change, especially at high energies. In the first example, the magnitude of the perturbation is small, and the semi-analytic approach still provides reasonably accurate estimates of the cross sections and integral parameters. In the case with low moderator density, the amplitude

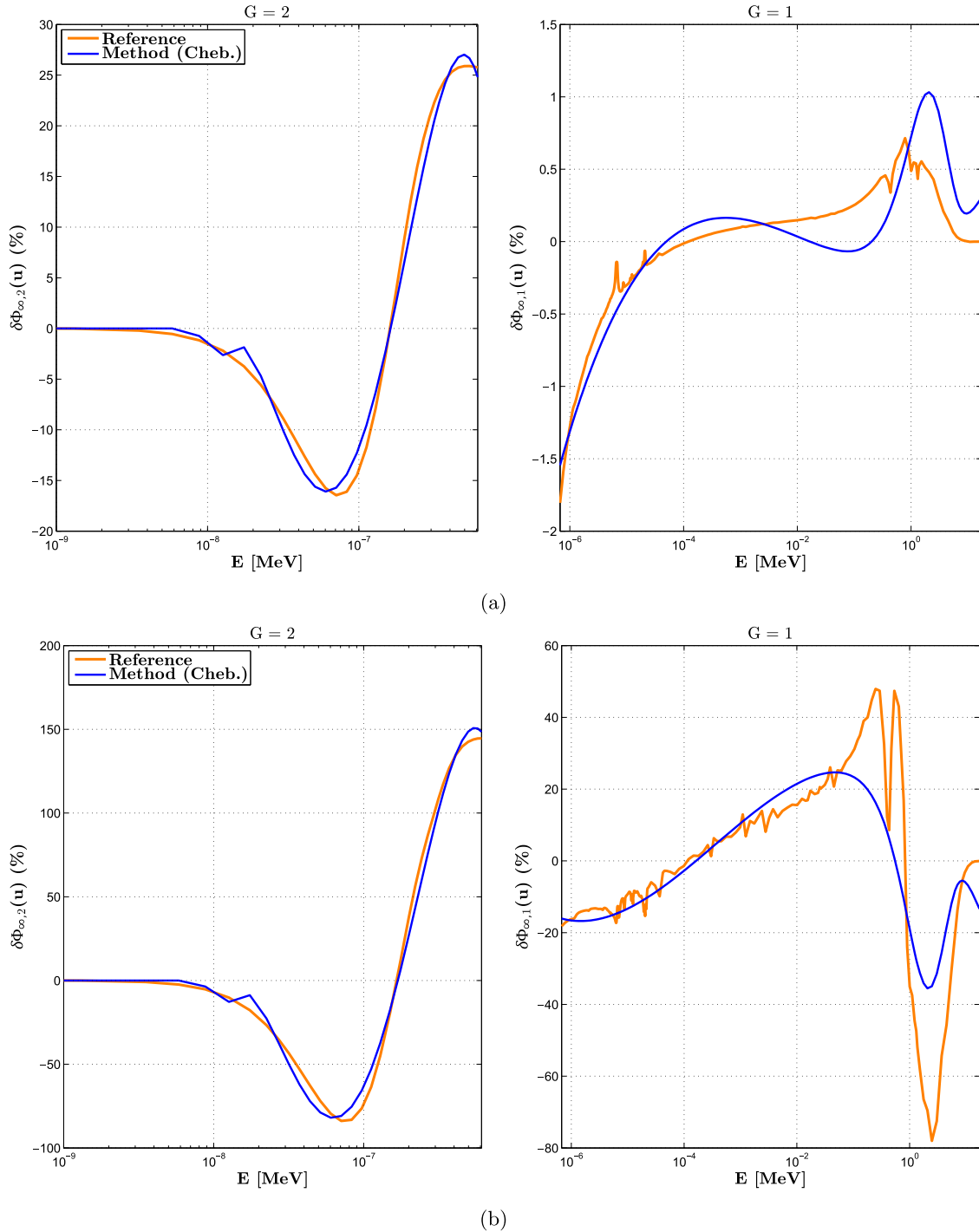


Fig. 26. Spectrum changes computed with the semi-analytic basis for the following transitions (without xenon variation): (a) from $C_{B_{10}} = 700$ ppm to $C_{B_{10}} = 2450$ ppm; (b) from $\rho_{H_2O} = 0.7$ g/cm³ to $\rho_{H_2O} = 0.21$ g/cm³.

Table 14

Examples with the semi-analytic basis: errors in the reconstructed macroscopic cross sections and in the main integral parameters, and number of iterations.

Perturbed state	$\Delta\Sigma_{a,1}^{\infty}$ (%)	$\Delta\Sigma_{a,2}^{\infty}$ (%)	$\Delta\nu\Sigma_{f,1}^{\infty}$ (%)	$\Delta\nu\Sigma_{f,2}^{\infty}$ (%)	$\Delta\Sigma_{s,1\rightarrow 2}^{\infty}$ (%)	Δk_{∞} [pcm]	$\Delta\Phi_{\infty,G}$ (%)	$\Delta\bar{P}_{fiss}^{\infty}$ (%)	n_{iter}
$C_{B_{10}} = 2450$ ppm	-0.096	0.257	0.190	0.215	-0.022	41	0.049, -0.224	0.032	8
$\rho_{H_2O} = 0.21$ g/cm ³	1.107	1.084	2.89	1.071	-1.645	-549	0.211, -2.52	0.602	14

of the deformation is high and the deviations in the computed curve result in a poor prediction of the nodal parameters. Thus, this set of modes cannot preserve in a generalized sense a degree of accuracy comparable to that of standard interpolation.

A basis function (such as a fission spectrum shifted toward lower values of E) could be added to better fit the high-energy double peak that characterizes water-density perturbations (Figs. 13 and 26). The first of the two peaks of opposite sign is centered at

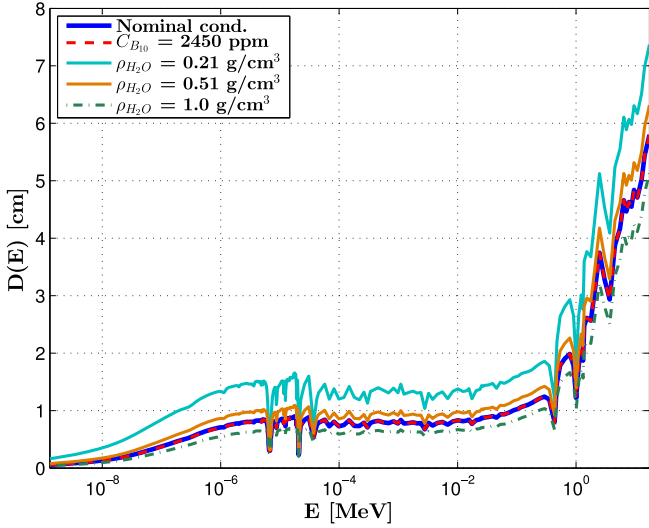


Fig. 27. Infinite-medium fine-group, homogenized diffusion coefficient of a 1.8%-enriched UO₂ assembly at different physical conditions. The xenon concentration is zero in conditions other than the nominal ones.

about 400 keV, which is the average energy of delayed neutrons (Stacey, 2007). Therefore, this additional mode may also be exploited to capture neutron-dynamics features in the simulation of reactor transients.

4.3. Reconstruction of the diffusion coefficient

The diffusion coefficient is reconstructed with a procedure similar to that described for the macroscopic cross sections. Fig. 27 depicts the fine-group diffusion coefficient in a 1.8%-enriched UO₂ lattice at different physical conditions. The distributions have been computed in APOLLO2-A with the outflow transport approximation (Choi et al., 2015). Along the whole energy domain, the impact of variations in the boron and xenon concentrations is negligible. Therefore, the corresponding microscopic-effect and cross corrections $\delta D_G^{\infty,m}$ and $\delta D_G^{\infty,*}$ (Eqs. (12c) and (12d)) can be neglected. Only the moderator density has a significant impact on the diffusion-coefficient energy distribution. We account for its effect via *ad hoc* macroscopic coefficients $s_{R,D,G,j}$ and $s_{V,D,G,i,j}$ (Eq. (29)), which are computed with a polynomial approximation in one variable as described in Section 2.1.2. Eq. (34) is then adapted to the diffusion coefficient as

$$h_{V,D,G,i,j}^{loc} \approx h_{V,D,G,i,j}^{nom} + s_{V,D,G,i,j} \quad (44)$$

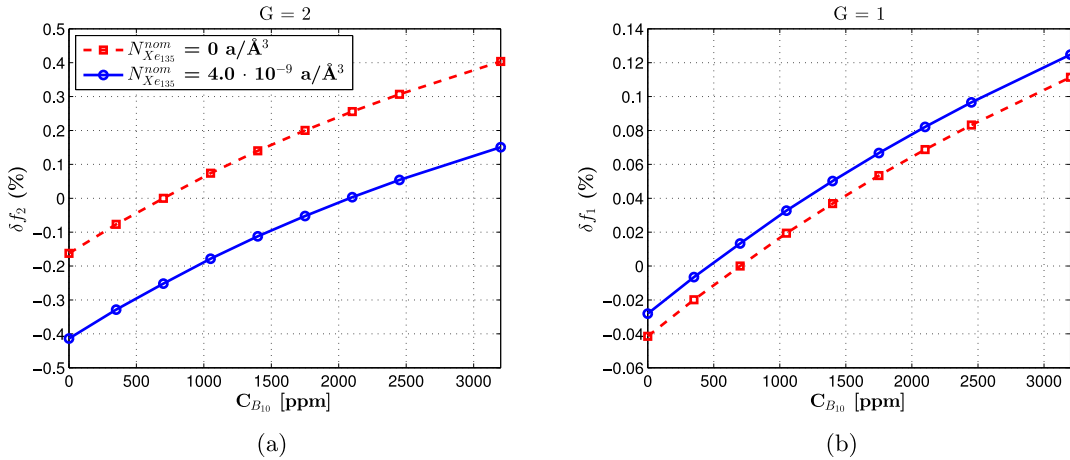


Fig. 28. Variations in the (a) thermal- and (b) fast-group assembly-surface discontinuity factors versus the concentration of soluble boron.

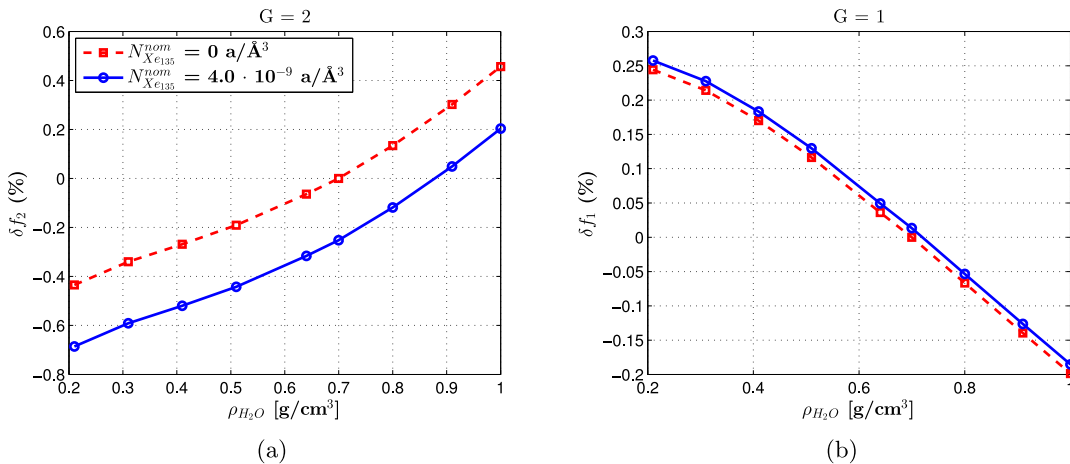


Fig. 29. Variations in the (a) thermal- and (b) fast-group assembly-surface discontinuity factors versus the water density.

where the rehomogenization parameters $h_{V,D,G,i,j}^{\text{nom}}$ are determined according to Eq. (18) with the nominal distribution $D_{\infty,G}^{\text{nom}}(u)$. Eq. (36) still holds for the few-group correction δD_G^{∞} .

It should be noted that, if the diffusion coefficient is computed via the fundamental-mode B_1 equations (Hebert, 2009), variations in the boron concentration and xenon density cause a change in its distribution in the high-energy region (at $E > 1$ MeV). This unphysical effect is due to an inherent limitation of the B_1 methodology (Smith, 2017), which produces an increase (or decrease) in the diffusion coefficient at all energies as the lattice reactivity decreases (or increases). Because of this behavior, the contributions of boron and xenon variations to the correction terms $\delta D_1^{\infty,m}$ and $\delta D_1^{\infty,*}$ (which we have set to zero in the test case of Section 3.2) may no longer be negligible.

4.4. On the discontinuity factors and form functions

We briefly discuss the impact of variations in ρ_{H_2O} , $C_{B_{10}}$ and $N_{Xe_{135}}$ on the assembly discontinuity factors and form functions. At the library preparation stage, the discontinuity factors are usually determined and stored at the same points of the state-parameter phase space as the nodal cross sections. The form-function model often uses a simplified approach. For instance, in ARTEMIS their multivariate dependence is built with only two two-parameter cross terms.

For the UO_2 bundle considered in Section 3.1, Figs. 28 and 29 show the variation in the assembly-surface discontinuity factors versus the boron concentration and the water density, respectively. Changes are small (mostly $< 0.2\%$ in the fast group and $< 0.5\%$ in the thermal one) along the whole range of values of the two state parameters. This is because discontinuity factors are meant to account for intra-assembly heterogeneity, whereas perturbations in the state parameters are homogeneous within a given node. Their influence on the intranodal flux distribution is limited to changes in the fuel-to-moderator flux ratio, for the reasons discussed in Section 2.1.2. This can be observed, for example, in Fig. 30(a), which shows the perturbation in the thermal-flux form function at $C_{B_{10}} = 0$ ppm and $N_{Xe_{135}} = 0$ a/Å³ with respect to the nominal state of Table 1. The variations observed in Figs. 28 and 29 are significantly smaller than those induced by neighbor effects in the core environment. For instance, Dall’Osso (2014) found changes (compared to the infinite-medium values) of about 1.0% and 3.0% in the fast- and thermal-group environmental discontinuity factors of a rodged UO_2 assembly neighboring an unrodged assembly of the same type. We have found even higher variations (up to 6.0%) at UO_2 /MOX interfaces.

Fig. 30(b) depicts the variation in the total-fission-power form function at $C_{B_{10}} = 0$ ppm and $N_{Xe_{135}} = 0$ a/Å³. A radial tilt is observed in the power spatial distribution. Higher perturbations in the flux and power form functions are found at very low moderator densities. For example, changes in the power distribution up to 2% occur in the assembly periphery at $\rho_{H_2O} = 0.21$ g/cm³. As observed for discontinuity factors, these variations are still modest compared to those induced by the spatial effects of the core environment.

In order to fully benefit from the reduction in the computational burden of the lattice calculation and in the library memory requirements, a method should be found to reproduce the effects of local nuclide density changes on the assembly discontinuity factors and form functions. We are currently working on an improved spatial rehomogenization model that may also address this aspect. This method aims to compute the variation in the 2-D spatial distribution of the neutron flux density between the real environment and the single-assembly conditions. Following an approach similar to that presented in this work (namely, computing the variation with respect to the infinite-lattice flux distribution in the nominal conditions), the spatial correction on the discontinuity factors could also include the state-parameter effect. Changes in the flux and power form functions may instead be estimated via empirical correlations.

4.5. Reconstruction of the B^2 -corrected single-assembly cross sections

In the approach presented in this work, the cross sections are reconstructed without the critical-buckling correction. If the critical-spectrum approximation is used, Eq. (16) becomes

$$\begin{aligned} \bar{\Phi}_{\infty,G}^{\text{loc}} h_{R,r,G,j}^{\text{loc}} + \sum_{i=1}^{N_{Q_G}} \alpha_{\infty,G,i} h_{V,r,G,i,j}^{\text{loc}} + c_{G_j}^{\infty,\text{loc}} \\ = \chi_{G,j} \sum_{G'=1}^{N_G} \left(\bar{\Phi}_{\infty,G'}^{\text{loc}} h_{R,f,G'}^{\text{loc}} + \sum_{i=1}^{N_{Q_{G'}}} \alpha_{\infty,G',i} h_{V,f,G',i}^{\text{loc}} \right) \\ + \sum_{\substack{G'=1 \\ G' \neq G}}^{N_G} \left(\bar{\Phi}_{\infty,G'}^{\text{loc}} h_{R,s,G'-G,j}^{\text{loc}} + \sum_{i=1}^{N_{Q_{G'}}} \alpha_{\infty,G',i} h_{V,s,G'-G,i,j}^{\text{loc}} \right), \end{aligned} \quad (45)$$

where $c_{G_j}^{\infty,\text{loc}}$ is the projection coefficient of the critical-leakage spectrum in the local conditions (see Eq. (14)):

$$c_{G_j}^{\infty,\text{loc}} = \int_0^1 du W_{G_j}(u) L_{\infty,G}^{\text{loc}}(u). \quad (46)$$

We express $L_{\infty,G}^{\text{loc}}(u)$ as

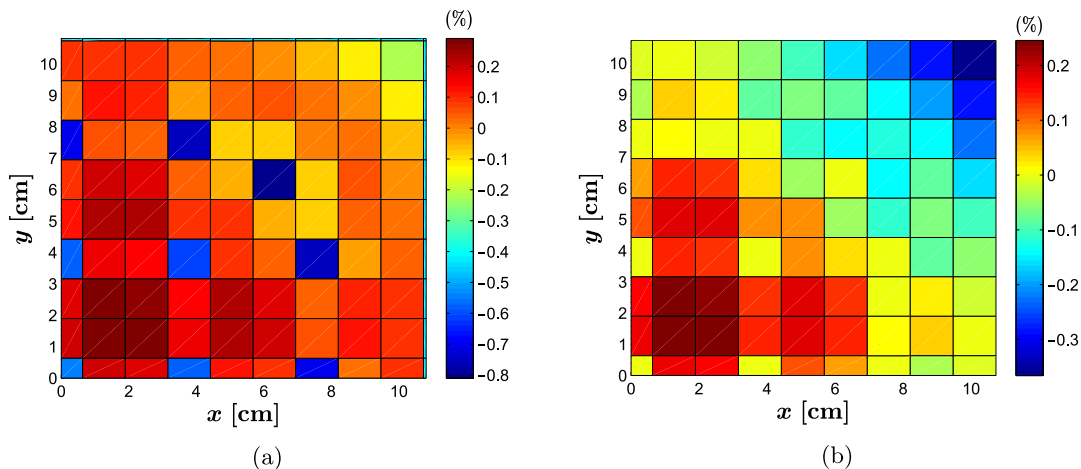


Fig. 30. Variation (in percentage) in the (a) thermal-flux and (b) total-fission-power form functions at $C_{B_{10}} = 0$ ppm and $N_{Xe_{135}} = 0$ a/Å³. The nominal values are those of Table 1.

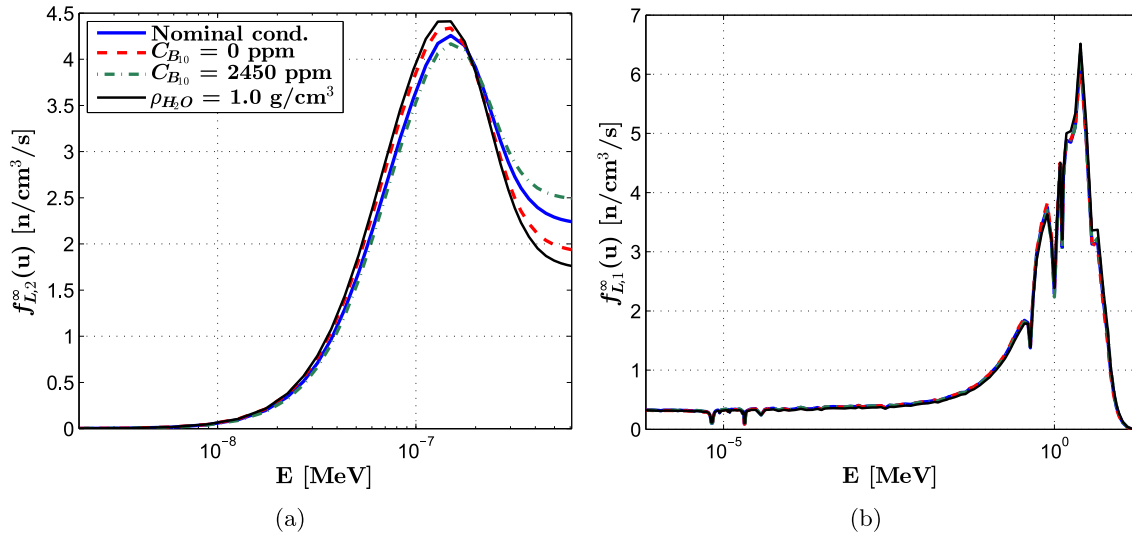


Fig. 31. (a) Thermal- and (b) fast-group fundamental-mode leakage spectra (normalized to unity) in the nominal state (Table 1) and in various perturbed conditions.

$$L_{\infty,G}^{\text{loc}}(u) = \bar{L}_{\infty,G}^{\text{loc}} f_{L,G}^{\infty,\text{loc}}(u), \quad (47)$$

where $\bar{L}_{\infty,G}^{\text{loc}}$ is the infinite-medium, coarse-group critical leakage, and $f_{L,G}^{\infty,\text{loc}}(u)$ is the fundamental-mode leakage spectrum normalized to unity (Gamarino et al., 2018b):

$$\bar{L}_{\infty,G}^{\text{loc}} = D_G^{\infty,\text{loc}} B_{\text{crit,loc}}^2 \bar{\Phi}_{\infty,G}^{\text{loc}}, \quad f_{L,G}^{\infty,\text{loc}}(u) = \frac{D_{\infty,G}^{\text{loc}} B_{\text{crit,loc}}^2 \psi_{\infty,G}^{\text{loc}}(u)}{\int_0^1 du D_{\infty,G}^{\text{loc}}(u) B_{\text{crit,loc}}^2 \psi_{\infty,G}^{\text{loc}}(u)}. \quad (48)$$

In Eq. (48), we have used the same notation as in Eq. (14). The few-group diffusion coefficient $D_G^{\infty,\text{loc}}$ comes from the latest iteration of the reconstruction algorithm (see Fig. 5 and Section 4.3), whereas $B_{\text{crit,loc}}^2$ and $\bar{\Phi}_{\infty,G}^{\text{loc}}$ are estimated solving the B^2 -variant of Eq. (20). For example, the critical zero-dimensional balance in the fast group reads

$$\left(\sum_{a,1}^{\infty,\text{loc}} + D_1^{\infty,\text{loc}} B_{\text{crit,loc}}^2 + \sum_{s,1 \rightarrow 2}^{\infty,\text{loc}} - \nu \sum_{f,1}^{\infty,\text{loc}} \right) \cdot \bar{\Phi}_{\infty,1}^{\text{loc}} = \left(\sum_{s,2 \rightarrow 1}^{\infty,\text{loc}} + \nu \sum_{f,2}^{\infty,\text{loc}} \right) \cdot \bar{\Phi}_{\infty,2}^{\text{loc}}. \quad (49)$$

Reconstructing the buckling-corrected cross sections requires the knowledge of $f_{L,G}^{\infty,\text{loc}}(u)$. A simple approach is to assume that its shape does not change significantly with the physical conditions in the node, namely

$$f_{L,G}^{\infty,\text{loc}}(u) \approx f_{L,G}^{\infty,\text{nom}}(u). \quad (50)$$

For the unrodded UO_2 fuel assembly considered in this work, Fig. 31 depicts the critical-leakage spectra in the nominal conditions of Table 1 and in few perturbed states, all of which have $N_{\text{Xe}_{135}} = 0 \text{ a}/\text{\AA}^3$. The differences between the local and nominal distributions are negligible in the fast group. However, the approximation of Eq. (50) is not warranted in the thermal range. The impact of this assumption has been quantified solving Eq. (45) in one step (i.e., without iterations). We have solved Eq. (49) with the two-group B^2 -corrected cross sections and diffusion coefficients interpolated at the local conditions (i.e., at the local values of $\rho_{\text{H}_2\text{O}}$, $C_{\text{B}_{10}}$, and $N_{\text{Xe}_{135}}$). The so obtained values of $\bar{\Phi}_{\infty,G}^{\text{loc}}$ and $B_{\text{crit,loc}}^2$ have been used in Eqs. (45) and (48). In this way, the approximation of Eq. (50) is the only source of inaccuracy in the solution of Eq. (45). For some perturbed states, Table 15 shows the error in the infinite-medium multiplication factor ensuing from this procedure. Significant devi-

Table 15

Error in the multiplication factor computed with a one-step reconstruction of the B^2 -corrected single-assembly cross sections. All cases have $N_{\text{Xe}_{135}} = 0 \text{ a}/\text{\AA}^3$.

Local conditions	Error [pcm]
$C_{\text{B}_{10}} = 0 \text{ ppm}$	−11
$C_{\text{B}_{10}} = 3000 \text{ ppm}$	205
$N_{\text{Xe}_{135}} = 0 \text{ a}/\text{\AA}^3$ ($C_{\text{B}_{10}}^{\text{nom}}, \rho_{\text{H}_2\text{O}}^{\text{nom}}$)	−32
$\rho_{\text{H}_2\text{O}} = 0.81 \text{ g/cm}^3$, $C_{\text{B}_{10}} = 1000 \text{ ppm}$	−13
$\rho_{\text{H}_2\text{O}} = 0.51 \text{ g/cm}^3$	−47
$\rho_{\text{H}_2\text{O}} = 0.21 \text{ g/cm}^3$	163

ations are found at low moderator densities and high boron concentrations. If the same one-step procedure is applied to the zero-buckling problem (Eq. (16)), the error in k_{∞} drops to 0 pcm in all sample cases. This outcome suggests that more complex modeling of $f_{L,G}^{\infty,\text{loc}}(u)$ is needed for an accurate reconstruction of the B^2 -corrected cross sections. A potential approach is to define the critical spectrum $\psi_{\infty,G}^{\text{loc}}(u)$ in Eq. (48) with Eqs. (9) and (15). However, this option would introduce an additional non-linearity in the rehomogenization algorithm.

5. Conclusions

We have proposed a novel method to model the spectral effects of local nuclide density changes on the nodal (macroscopic and microscopic) cross sections. The cross-section multivariate dependence on the water density, the concentration of diluted boron and the xenon level is reproduced with a rehomogenization-based approach. Our target accuracy is achieved in most of the phase space of these three state parameters. Deviations close to or slightly higher than the prescribed error bounds are only found in fast-group cross sections at very low moderator densities (below 0.3 g/cm^3), which can be experienced in accidental conditions. However, these deviations are still small compared to the homogenization errors commonly found in standard nodal simulations of strongly heterogeneous multi-assembly configurations.

Eventually, the rehomogenization algorithm inherently predicts the combined spectral changes due to (i) variations in the local physical conditions, (ii) interassembly neutron leakage, and (iii) different reactivity in the real environment and in the infinite lattice. These findings lay the groundwork for a new concept of

cross-section model, featuring (i) a considerably smaller number of branch calculations in the lattice-physics code and of table points in the parameterized libraries, and (ii) a computationally less demanding on-line reconstruction of the nodal cross sections.

Future work will include the validation of the methodology on other types of fuel assemblies (such as MOX and Pyrex- or gadolinium-bearing assemblies) and on calculations with depletion, in both infinite-medium and environmental conditions. Another topic to be addressed is modeling the spectral effects of the local physical conditions on the assembly discontinuity factors and form functions.

Acknowledgment

This work was supported by the Framatome Ph.D. program.

References

- Bahadir, T., Lindahl, S., 2009. Studsvik's next generation nodal code SIMULATE-5. Proc. of Advances in Nuclear Fuel Management IV (ANFM 2009), Hilton Head Island, South Carolina, USA, April 12–15.
- Bahadir, T., Lindahl, S., Palmtag, S.P., 2005. SIMULATE-4 multigroup nodal code with microscopic depletion model. Proc. of Mathematics and Computation, Supercomputing, Reactor Physics and Nuclear and Biological Applications (M&C 2005), Avignon, France, September 12–15.
- Bilodid, I., Mittag, S., 2010. Use of the local Pu-239 concentration as an indicator of burnup spectral history in DYN3D. Ann. Nucl. Energy 37 (9), 1208–1213.
- Bokov, P.M., 2009. Automated few-group cross-section parameterization based on quasi-regression. Ann. Nucl. Energy 36 (8), 1215–1223.
- Bokov, P.M., Prinsloo, R.H., 2007. Cross-section parameterization using quasi-regression approach. Proc. of Joint International Topical Meeting on Mathematics & Computation and Supercomputing in Nuclear Applications (M&C+ SNA 2007), Monterey, California, USA, April 15–19.
- Bokov, P.M., Prinsloo, R.H., Tomašević, D.I., Reitsma, F., 2008. A quasi-regression method for automated cross-section parameterization: PBMR benchmark example. Proc. of Int. Conf. PHYSOR 2008, Interlaken, Switzerland, September 14–19.
- Bokov, P.M., Botes, D., Zimin, V.G., 2012. Pseudospectral Chebyshev representation of few-group cross sections on sparse grids. Proc. of Int. Conf. PHYSOR 2012, Knoxville, Tennessee, USA, April 15–20.
- Botes, D., Bokov, P.M., 2011. Hierarchical, multilinear representation of few-group cross sections on sparse grids. Proc. of Int. Conf. on Mathematics and Computational Methods Applied to Nuclear Science and Engineering (M&C 2011), Rio de Janeiro, RJ, Brazil, May 8–12.
- Botes, D., Bokov, P.M., 2014. Polynomial interpolation of few-group neutron cross sections on sparse grids. Ann. Nucl. Energy 64, 156–168.
- Botes, D., Chifamba, S., Bokov, P.M., 2017. A study of the performance of a sparse grid cross section representation methodology as applied to MOX fuel. Ann. Nucl. Energy 99, 444–454.
- Choi, S., Smith, K.S., Lee, H.C., Lee, D., 2015. Impact of inflow transport approximation on light water reactor analysis. J. Comput. Phys. 299, 352–373.
- Dall'Osso, A., 2014. Spatial rehomogenization of cross sections and discontinuity factors for nodal calculations. Proc. of Int. Conf. PHYSOR 2014, Kyoto, Japan, September 28 – October 3.
- Dall'Osso, A., Tomatis, D., Du, Y., 2010. Improving Cross Sections via Spectral Rehomogenization. Proc. of Int. Conf. PHYSOR 2010, Pittsburgh, Pennsylvania, USA, May 9–14.
- Duderstadt, J.J., Hamilton, L.J., 1976. Nuclear Reactor Analysis. John Wiley & Sons.
- Dufek, J., 2011. Building the nodal nuclear data dependences in a many-dimensional state-variable space. Ann. Nucl. Energy 38 (7), 1569–1577.
- Gamarino, M., Tomatis, D., Dall'Osso, A., Lathouwers, D., Kloosterman, J.L., van der Hagen, T.H.J.J., 2016. Investigation of Rehomogenization in the Framework of Nodal Cross Section Corrections. Proc. of Int. Conf. PHYSOR 2016, pages 3698–3707, Sun Valley, Idaho, USA, May 1–5.
- Gamarino, M., Dall'Osso, A., Lathouwers, D., Kloosterman, J.L., 2018a. Rehomogenization of nodal cross sections via modal synthesis of neutron spectrum changes. Nucl. Sci. Eng. 190 (1), 1–30.
- Gamarino, M., Dall'Osso, A., Lathouwers, D., Kloosterman, J.L., 2018b. A neutron-leakage spectrum model for on-the-fly rehomogenization of nodal cross sections. Ann. Nucl. Energy 116, 257–279.
- Guillo, M., Calloo, A., Couyras, D., Févotte, F., Brosselard, C., Bouriquet, B., Dubois, A., Girardi, E., Hoareau, F., Fliscounakis, M., Leroyer, H., Noblat, E., Pora, Y., Plagne, L., Ponçot, A., Schwartz, N., 2017. COCAGNE: EDF new neutronic core code for ANDROMÈDE calculation chain. Proc. of Int. Conf. on Mathematics and Computational Methods Applied to Nuclear Science and Engineering (M&C 2017), Jeju, Korea, April 16–20.
- Hebert, A., 2009. Applied reactor physics. Presses Internationales Polytechnique.
- Hobson, G., Bolloni, H.W., Breith, K.A., Dall'Osso, A., van Geemert, R., Haase, H., Hartmann, B., Leberig, M., Porsch, D., Pothet, B., et al., 2013. ARTEMIS™ core simulator: Latest developments. In: Joint International Conference on Supercomputing in Nuclear Applications + Monte Carlo, Paris, France, October 27–31, EDP Sciences.
- Lamarsh, J.R., 1966. Introduction to nuclear reactor theory. Addison-Wesley.
- Lawrence, R.D., 1986. Progress in nodal methods for the solution of the neutron diffusion and transport equations. Prog. Nucl. Energy 17 (3), 271–301.
- Luu, T.H., Maday, Y., Guillo, M., Guérin, P., 2017. A new method for reconstruction of cross-sections using Tucker decomposition. J. Comput. Phys. 345, 189–206.
- Martin, N., Riedmann, M., Bigot, J., 2017. Latest Developments in the ARTEMIS™ Core Simulator for BWR Steady-state and Transient Methodologies. Proc. of Int. Conf. on Mathematics and Computational Methods Applied to Nuclear Science and Engineering (M&C 2017), Jeju, Korea, April 16–20.
- Martinolli, E., Carter, T.C., Clement, F., Demy, P.M., Leclere, M., Magat, P., Marquis, A., Marotte, V., Schneider, M., Villatte, L., et al., 2010. APOLLO2-A - AREVA's new generation lattice physics code: methodology and validation. Proc. of Int. Conf. PHYSOR 2010, Pittsburgh, Pennsylvania, USA, May 9–14.
- Sanchez, R., 2009. Assembly homogenization techniques for core calculations. Prog. Nucl. Energy 51 (1), 14–31.
- Sánchez-Cervera, S., García-Herranz, N., Herrero, J.J., Cabellos, O., 2014. Optimization of multidimensional cross-section tables for few-group core calculations. Ann. Nucl. Energy 69, 226–237.
- Smith, K.S., 1986. Assembly homogenization techniques for Light Water Reactor analysis. Prog. Nucl. Energy 17 (3), 303–335.
- Smith, K.S., 2017. Nodal diffusion methods and lattice physics data in LWR analyses: Understanding numerous subtle details. Prog. Nucl. Energy 101, 360–369.
- Stacey, W.M., 2007. Nuclear Reactor Physics. John Wiley & Sons.
- Turski, R.B., Morris, E.E., Taiwo, T.A., Cahalan, J.E., 1997. Macroscopic cross section generation and application for coupled spatial kinetics and thermal hydraulics analysis with SAS-DIF3DK. Proc. of Joint international conference on mathematical methods and supercomputing in nuclear applications, Saratoga Springs, New York, USA, October 6–10.
- van Geemert, R., 2014. A multi-level surface rebalancing approach for efficient convergence acceleration of 3D full core multi-group fine grid nodal diffusion iterations. Ann. Nucl. Energy 63, 22–37.
- Watson, J.K., Ivanov, K.N., 2002. Improved cross-section modeling methodology for coupled three-dimensional transient simulations. Ann. Nucl. Energy 29 (8), 937–966.
- Zimin, V.G., Semenov, A.A., 2005. Building neutron cross-section dependencies for few-group reactor calculations using stepwise regression. Ann. Nucl. Energy 32 (1), 119–136.